A LARGE PALEOEARTHQUAKE IN THE CENTRAL APENNINES, ITALY, RECORDED BY THE COLLAPSE OF A CAVE SPELEOTHEM

Bruno Pace (1,6), Alessandro Valentini (1), Luigi Ferranti (2,6), Marcello Vasta (3), Maurizio Vassallo (4), Paolo Montagna (5), Abner Colella (2), Edwige Pons-Branchu (7)

(1) DISPUTER - Università degli studi Gabriele d'Annunzio, Chieti, Italy

(2) DiSTAR - Dipartimento di Scienze della Terra, dell'Ambiente e delle Risorse Università di Napoli "Federico II"

(3) INGEO - Università degli studi Gabriele d'Annunzio, Chieti e Pescara, Italy

(4) Istituto Nazionale di Geofisica e Vulcanologia, sezione di Roma1, sede di L'Aquila, Italy

(5) Institute of Polar Sciences, ISMAR-CNR, Bologna, Italy

(6) CRUST - Centro inteRUniversitario per l'analisi SismoTettonica tridimensionale con applicazioni territoriali, Italy

(7) Laboratoire des Sciences du Climat et de l'Environnement, LSCE/IPSL, CEA-CNRS-UVSQ, Université Paris-Saclay, Gif-sur-Yvette, France

Abstract

Speleoseismological research carried out in the Central Apennines (Italy) contributed to understanding the behaviour of active normal faults that are potentially able to generate M 6.5–7 earthquakes documented by paleoseismology and by historical and instrumental seismology. Radiometric (U-Th, AMS-^{14}C, and bulk-^{14}C) dating of pre- and post- deformation layers from collapsed speleothems found in Cola Cave indicates that at least three speleoseismic events occurred in the cave during the last ~12.5 ka and were ostensibly caused by seismic slip on one or more of the active faults located in the region surrounding the cave. We modelled the collapse of a tall (173 cm high) stalagmite to find a causative association of this event with one among the potential seismogenic sources. We defined the uniform hazard spectrum (*UHS*) for each seismogenic source at the site and we used the calculated spectra in a deterministic approach to study the behavior of the speleothem, through a numerical finite element modelling (*FEM*). Although our analysis suggests the *"Liri"* fault as the most likely source responsible for the ground shaking recorded in the cave, the *"Fucino"* fault system, responsible for a M 7 earthquake in 1915, cannot be excluded as a potential source of speleoseismic damage. Results of this work provide new constraints on the seismotectonic history of this sector of Central Apennines and highlight the performance of integrated speleoseismological, seismic hazard and numerical studies.

Keywords*: Speleoseismology; Central Apennines; Seismic Hazard; Finite Element Modelling*

1. Introduction

Cave speleothems can be used not only for paleoenvironmental and paleoclimatic reconstructions (Gascoyne et al., 1980; Li et al., 1989; Talma & Vogel, 1992; Lauritzen, 1995; Bar-Matthews et al., 1999; McDermott, 2004), but also for speleoseismological research, i.e. the investigation of traces of ancient earthquakes in caves (Kagan et al., 2005; Becker et al., 2006). Since the 80's researchers (e.g. Forti & Postpischl, 1980; Forti et al., 1981; Forti & Postpischl, 1984; Postpischl et al., 1991, Forti, 2001, Rajendran et al., 2016) established that in the proved absence of other deformation sources (landslide, flooding, ice flow, animal or anthropic passage), the deviation of the growth axis from the vertical and the speleothem collapse are evidence for seismic shaking of cave walls. Improvements in analytical techniques and theoretical modelling also showed that in earthquake-prone regions, unbroken speleothems that have survived all the earthquakes occurred during their life span may provide constraints on seismic hazard estimates, allowing to extend the window of observation of a given historical catalogue (Di Domenica & Pizzi, 2017; Gribovski et al., 2013, 2018; Ferranti et al., 2019).

In terms of seismic hazard, the main issue concerns the evaluation of the ground motion potentially responsible (or not) of the speleothems collapse. Cadorin et al. (2001) carried out laboratory measurements on stalagmite samples to study their failure in bending and estimate the ground acceleration necessary to break speleothems. Similarly, Lacave et al. (2000, 2004) investigated the mechanical behaviour of speleothems via static bending tests and estimated the probability that at least one moderate earthquake has occurred in the past. Recently, Mendecki and Szczygieł (2019) provided quantitative relationships between speleothems shape and their oscillation and acceleration during shaking. In these studies, the underlying idea is based on the stalactite-stalagmite oscillatory system, which represents the vertical datum. However, the difficulty in quantitative modelling of the observed deformation and its direct attribution to a seismogenic source remains a major issue (Lacave et al., 2004; Becker et al., 2006, Ferranti et al., 2019).

The aim of the present work is to reconstruct the speleoseismological history of Cola Cave (Abruzzo region, Central Italy, Figure 1) and to investigate the causes that led to the collapse of a tall (173 cm high) speleothem found in the cave. We were motivated to establishing whether this collapse represents the record of a large paleoearthquake, and how this and other speleoseismic event that we found in the cave are framed in the seismotectonic context of the Central Apennines.

Cola Cave is located in the internal sector of the Central Apennines (Figure 1), an area presently affected by NE-SW trending geodetic extension at 2-3 mm/yr (Devoti et al., 2011; D'Agostino, 2014; Cheloni

et al., 2017). Extension is accommodated by systems of NW-SE striking normal faults (Figure 1; Boncio et al., 2004; Pace et al., 2006; Valentini et al., 2017). The present activity of most Central Apennines faults is constrained by several evidence, and a number of them are considered seismogenic sources potentially able to generate M 6.5–7 earthquakes (Pace et al., 2006, 2010; Verdecchia et al., 2018; DISS Working Group, 2015) documented in the Central Apennines (Figure 1; Boncio et al., 2004; Galli et al., 2008; Chiaraluce et al., 2011).

Although a good age record exists for Late Pleistocene-Holocene earthquake slips from fault scarp analysis (e.g. Galadini & Galli, 2000; Roberts & Michetti, 2004; Schlagenhauf et al., 2011), and trench paleoseismology (e.g. Cinti et al., 2011; Galli et al., 2008) on the major Central Apennines faults, there are still contrasting views about the capability of several faults to generate earthquakes.

2. Seismotectonic context

Cola cave is surrounded by major active faults and the region has been shaken by large earthquakes, the largest of them occurred over the last century (Fucino 1915 Mw 7; L'Aquila 2006 Mw 6.3; Central Italy 2016 Mw 6.5). The active faults are mainly south west-dipping normal faults and are organised in fault systems. Some of them are considered seismogenic (Boncio et al., 2004; Valentini et al., 2017) (red traces in Figure 1).

The most important fault system is the "Fucino" (source n. 2 in Figure 1), whose activity controlled the growth of the largest intermontane basin in the Central Apennines during the last ~2-3 Ma. The ~ 38 km-long surface expression of the Fucino fault system (Galadini and Galli, 1999) is represented, from north to south, by three main fault segments, namely the Magnola fault (MF, Figure 1), the Marsicana Highway-Parasano fault (MHP, Figure 1) and the San Benedetto dei Marsi-Gioia dei Marsi fault (SBGM, Figure 1) (e.g. Serva et al., 1986; Giraudi, 1988; Michetti et al., 1996; Messina, 1996). The 1915 earthquake activated most of the Fucino source producing coseismic ground displacements up to about 1 m high, as described by Oddone (1915) and confirmed by paleoseismological studies (Serva et al., 1986; Michetti et al., 1996; Galadini et al., 1997; Galadini & Galli, 1999). The paleoseismic trenches revealed at least seven additional surface rupture events during the last ~20 ka with offsets comparable to the 1915 earthquake slip (Galli et al., 2008)., Galli et al. (2012) found trench evidence of recent activity of the MF segment, with one or more faulting events that have affected the Neoglacial colluvia (post 4.5 ka) before Roman age (~2 ka) deposits. The time span of this event roughly matches the 3.4±0.3 ka age of the penultimate exhumation event found on the fault scarp using the cosmogenic ^{36}Cl method (Schlagenhauf et al., 2010).

The *"Velino"* seismogenic source (source n. 4 in Figure 1) is located north of the Fucino basin and is represented by a bedrock scarp along the southern slope of Mt. Velino. The fault is considered currently active (Bosi, 1975; Boncio et al., 2004) as evidenced by geomorphological and paleoseismological

observations (Giraudi, 1992, Pace et al., 2008). Schlagenhauf et al. (2011) carried out cosmogenic ^{36}Cl dating of carbonate samples from the exhumed fault plane, reconstructing the slip history over the last 7.5 ka. They recognized five exhumation events with the last occurred around 1.3±0.3 ka. A single earthquake is assigned to the structure in the historical catalogue (CPTI15; Rovida et al., 2016, 2020), the event of 24/02/1904 (I_0 VIII-IX MCS; M_w 5.7).

The *"Salto Valley"* fault (source n. 3 in Figure 1) is a nearly 28 km long structure bordering the north-east side of the Salto Valley. Some authors believe that the fault is currently active (Roberts & Michetti, 2004; Papanikolaou et al., 2005) on the basis of morphological indications, while according to others fault activity ended at the beginning of the middle Pleistocene (Galadini & Messina, 2001).

The *"Campo Felice-Ovindoli"* fault system (source n. 1 in Figure 1) is characterised by several segments that form a single seismogenic source. The recent activity of the fault system is supported by paleoseismological studies realised on the different segments (e.g. Pantosti et al., 1996; Salvi et al., 2003). Three events that displaced Holocene deposits with a recurrence interval of about 3000 years were identified on the southern segment. The last event occurred in a time interval between 700-1130 years BP (Pantosti et al., 1996). Moreover, the event of 9 September 1349 (Mw 6.3, Rovida et al., 2016) has been attributed to the *"Campo Felice-Ovindoli"* seismogenic source activity (Pace et al., 2006).

Finally, the Cola cave is localised exactly along the ~60 km long *"Liri"* fault system. While the southern segment (Sora fault, about 20 km long) shows possible signs of seismic activity (Val Roveto earthquake, 1922, M_W 5.2), the activity of the central-northern sector (about 40 km long, source n. 5 in Figure 1) is still a matter of debate. Galadini & Messina (2004) consider the fault inactive, because of the lack of clear displacement of late Quaternary deposits and suggest that slip occurred during the late Pliocene-Middle Pleistocene. Roberts & Michetti (2004) studied the along strike variation of vertical dislocation and escarpment height of the fault. Assuming that these two parameters are congruous with the values measured on other active faults in central Apennines, they concluded that exposure of the fault surface is due to tectonic displacement and not to erosional exhumation.

The choice of Cola cave, for its strategic position in this complex seismotectonic context, may help to better constrain the paleoseismological record of active faults of the region, and to explore the activity of doubtful faults, such as the *"Liri"* fault, whose contribution to seismic hazard and seismic risk models could nevertheless be notable (Scotti et al., 2020).

3. Cave morphology

Cola cave opens at an elevation of ~1400 m a.s.l. on the south-west side of Mt. Arunzo, a culmination of a ~ 15 km long ridge belonging to the M.ti Carseolani mountain group. The ~200 m long cave is developed within thick Cretaceous limestone beds that cap a succession of Mesozoic platform

carbonates.

A narrow entrance carved along less competent limestone and marly beds (point *A*, Figure 2) leads to a large sub-rectangular (~60x30 m), ~5-10 m high room occupied by fallen ceiling blocks which reach dimensions up to a few m^3 (point *B*, Figure 2). A steep (20° average) northwest-southeast trending slope brings to the more internal part of room *B* where large speleothems and columns are grown upon ancient rockfalls. Here, the cave turns to follow a northeast-southwest trend. To the northeast, the cave again bifurcates (point *C*, Figure 2). The main branch continues towards northeast across rooms rich of concretions (point *D*, Figure 2), whereas a narrower branch detaches to the east and terminates in a circular room with a small ephemeral lake (point *E*, Figure 2). To the southwest of the main room, the cave progressively descends getting narrower, and reaches a series of small rooms decorated by abundant speleothems and pools (point *F*, Figure 2). The cave continues deepening to the southwest through tighter passages and shafts, but we did not explore this section further.

4. Material and Methods

The research methodology integrates:

- field work in the cave, which includes structural analysis aimed to exclude that the observed speleothem deformation is the result of local non-tectonic processes, measurement of the geometry of collapsed speleothems, and collection of samples from fallen and regrown speleothems to constraint events age;
- laboratory work, consisting in (^{230}Th/U) and AMS-^{14}C dating of pre- and post-event layers;
- seismic hazard analysis, to define a seismogenic source model and calculate the expected ground motion at the site in terms of uniform hazard spectra;
- numerical modelling of a selected fallen stalagmite, to study the speleothem behaviour during the passage of the expected seismic waves, and to estimate the possible seismogenic source of the recorded speleoseismic event.

4.1 Speleothem sampling and cave structural analysis

We measured the geometry of 29 collapsed speleothems using a tape and sampled by hammer a selection of them for radiometric dating and geo-mechanical tests. For each measured speleothem, we recorded the length and the average diameter of the fallen section. For stalagmites, we also tried to recognize the standing stump from which the speleothem fall. Commonly, the stump narrows upwards to form a neck of the pre-failure stalagmite. Indeed, when a large earthquake occurs in the vicinity of the

cave, the speleothems oscillate due to the ground motion until its failure tensile stress may be overcome and the speleothem breaks in the weakest part, the neck (Figure 3a, and 3b). Because the stalagmite neck is characterized by a change in orientation of C axes of calcite crystals from horizontal at the base to vertical above (P. Forti, personal communication, 1999), it represents the weakest section and the potential locus of breakage during seismic shaking (Figure 3b; Lacave et al., 2004).

Based on cave topography and on the geomorphological setting (relative ease of access), we cannot exclude in principle that the observed speleothem deformation is the result of non-tectonic processes such as water flooding, flow of ice during past glacial stages, and animal or anthropic passage (Becker et al., 2012; Jaillet et al., 2006; Kagan et al., 2005, 2017). All the above processes are expected to produce a random orientation of fallen speleothems. Conversely, during seismic shaking, it Is predicted that speleothems fall to the ground along a direction broadly aligned with the mean direction of the seismic waves (Figure 3b). To disentangle between a tectonic versus a non-tectonic origin for the observed collapses, we measured the fall azimuth of 29 stalagmites. The azimuth distribution clusters along the NNW-SSE direction, with minor petals to the WSW and NNE (Figure 2). The tight azimuthal distribution argues for a tectonic origin, inasmuch it is roughly parallel with the mean strike of the seismogenic sources of the area (Figure 1).

Finally, we sampled both the tip of fallen speleothem and in few cases the base of speleothems grown on the top of the collapsed ones, to tightly constrain the age of the collapses (Figure 3c). In some cases, if the speleothem is not vulnerable enough, instead of collapsing, it could change its growth axis. In this case the evidences of earthquakes are in the inner structure of it (Figure 3d). Indeed, the youngest layer of a fallen speleothem and the base of an intact stalagmite grown upon it represent the pre-event and post-event layers, respectively (Forti & Postpischl, 1984; Becker et al., 2012; Kagan, 2012; Kagan et al., 2005). When the growth of an intact speleothem was not observed above a collapsed speleothem, we only took its youngest, pre-event layer.

4.2 Radiometric dating

Field samples were sawed in half to identify the layers for dating. Subsamples were extracted from the chosen laminae of stalagmites and stalactites using a dental drill with diamond-encrusted blades.

Both the U-series decay (^{230}Th/U) and AMS-^{14}C dating techniques were used to date nine samples (Figures 2 and 4). The ages of five samples were accurately determined by U/Th at the Laboratoire des Sciences du Climat et de l'Environnement (LSCE) at Gif-sur-Yvette, France using a ThermoScientific Neptune^{Plus} multi-collector inductively coupled plasma-mass spectrometer following the protocol developed at LSCE (Columbu et al., 2015; Pons-Branchu et al., 2014). Details of the analytical procedure for U/Th can be found in Ferranti et al. (2019). An initial ^{230}Th/^{232}Th activity ratio of 1.50±0.75 (Hellstrom, 2006)

was used to correct for the non-radiogenic detrital ^{230}Th fraction (Table 1). Four samples were AMS-^{14}C dated at the Center of Applied Physics, Dating and Diagnostics (CEDAD) Laboratory of the University of Salento, Italy (three samples) and at Beta Analytic, Inc. (one sample). Following Ferranti et al. (2019), the radiocarbon ages were first corrected for the "dead carbon portion" (DCP) and then converted to calendar years (cal. yr BP, BP = AD 1950) using the IntCal13 calibration curve (Reimer et al., 2013) and the Calib 7.10 program (Stuiver et al., 2020). Based on the DCP calculated in Ferranti et al. (2019), we used values of 5% and 10% (Table 2), which translates to a difference between DCP-corrected and DCP-uncorrected ^{14}C ages of approximately 10-20%. As a preferred age, we consider for each sample the average between the calibrated ages and related uncertainty range from the 5% and 10% DCP-corrected ages and uncertainty (Table 2).

4.3 Seismic hazard analysis

We carried out a seismic hazard analysis to model the impact of past large earthquakes generated by faults located in the surroundings of Cola cave. We defined the uniform hazard spectrum (*UHS*) for each seismogenic source at the investigation site. We used the calculated spectra in a deterministic approach to study the behaviour of COLA-3 speleothem (from which COLA-3 sample was taken for dating), found fallen from its stump in Room *D* (Figure 2), through a numerical finite element modelling (*FEM*). The approach permits to estimate which seismogenic source(s) were potentially responsible of the speleothem collapse.

We selected COLA-3 (Figure 4b-c) because (i) the azimuth of the fall (N355°E±3) is consistent with the general NNW-SSE pattern of measured falls (Figure 2) arguing for a tectonic origin of the collapse; and (ii) we were able to date both the last pre-collapse (COLA-3) layer of the stalagmite and the initial post-collapse layer of two small stalagmites grown above its stump (COLA-1 and COLA-2, Figure 4b-c). We reconstructed the pre-collapse geometry of COLA-3 (Figure 5), which, considering the stump, was 1.73 meters tall, has an average section of 0.34 meters, wider at the base (up to ~0.46 meters) and narrows towards the tip (up to ~0.07 meters). In particular, the ~0.2 m tall stump shrinks at the top where it is ~30 cm wide, and probably this feature was a weak point along COLA-3 axis.

We carried out the seismic hazard analysis in three steps: 1) seismic noise measurements to quantify possible amplification phenomena; 2) definition of a seismogenic source model in the area surrounding the cave; and 3) definition of the uniform hazard spectra to be used for the numerical modelling.

First, three single stations seismic noise measurements were acquired in different rooms of Cola cave (COL1 and STR1 stations, Figure 2) and just outside the cave (OUT1 station, Figure 2). The stations were equipped with a Lennartz 5 s velocimeter and a 24-bit Reftek 130 digitizer. Each station acquired a continuous time window of noise of at least 1 hour long. The seismic data were used to evaluate the

246 resonance frequency of measurement sites and to quantify possible amplification phenomena. For this
247 purpose, the seismic noise was used to compute the spectral ratio (H/V) of the horizontal component
248 respect to the vertical (Bonnefoy-Claudet et al., 2006). H/V curves were computed at each site using the
249 free software Geopsy (Wathelet et al., 2020; www.geopsy.org). The analysis was performed starting from
250 the continuously recorded data divided using a 40 s long moving time-window. An anti-trigger software was
251 used to remove the windows with short transient which could be produced by anthropic activities, local
252 seismic events or rockfalls. For each accepted time window, we removed the mean, the linear trend and
253 applied a 5% cosine taper. Then, we computed the Fourier Amplitude Spectra (FAS) and smoothed the
254 amplitudes following the method proposed by Konno & Omachi (1998), using a coefficient of 40 for the
255 bandwidth. The two horizontal spectra were combined with the geometrical mean and finally divided by
256 the vertical spectrum to get the H/V ratios.
257 We used a seismogenic source model that summarizes and updates the knowledge of active
258 tectonics in the inner part of the Central Apennines (Galadini & Messina, 2004; Galadini & Galli, 2000;
259 Boncio et al., 2004; Pace et al., 2006; Valentini et al., 2017). We used a distance threshold of 50 km,
260 corresponding approximately to an expected ground shaking of ~ 0.25 g (PGA) from the known seismogenic
261 sources, beyond which we consider the effect of seismogenic sources negligible for the seismic hazard in
262 the area. We defined five seismogenic sources (Figure 1), namely *"Campo Felice-Ovindoli"* (1), *"Fucino"* (2),
263 *"Salto Valley"* (3), *"Velino"* (4) and *"Liri"* (5), representative of as many southwest-dipping active normal
264 faults. The length of the sources ranges between ~ 11 (source n.4) and ~ 38 km (source n.2), and the
265 seismogenic thickness is 11-15 km. The seismogenic source geometry has been parameterized using
266 published data (Pace et al., 2014; Peruzza et al., 2011; Faure-Walker, 2014; Valentini et al., 2019; Table 3).
267 For the *"Liri"* source, we modelled the northern sector, for a total length of 27 km suggested by
268 geomorphological considerations (Faure-Walker, 2014) and by aspect ratio relationships (Peruzza & Pace,
269 2002). We did not incorporate the southern sector of the fault because the cave is too far from it and
270 would lay in its footwall, less prone to seismic shaking.
271 We used kinematic, geometric, and slip rate information for each source as inputs for the *FiSH*
272 code (Pace et al., 2016) to calculate the global budget of the seismic moment rate allowed by the structure.
273 This calculation is based on predefined size-magnitude relationships in terms of the maximum expected
274 magnitude (M_{max}) and associated mean recurrence time (T_{mean}). The M_{max} values have been calculated using
275 different empirical relationships, benchmarked against observed magnitudes when available, following the
276 approach suggested by Pace et al. (2016). Results define a M_{max} ranging from M_w 6.1 (source n.4) to M_w 6.8
277 (source n.2) (Table 3).
278 Once the maximum expected magnitudes (M_{max}) for each source was computed, the OpenQuake
279 Engine software (Pagani et al., 2014) was used to calculate the Uniform Hazard Spectra (*UHS*) for the
280 following finite element modelling. The spectra were calculated at the cave site using two different ground

motion prediction equations (*GMPE*; Bindi et al., 2011; Cauzzi et al., 2015). These two *GMPE*s have been chosen because they use two different metrics: the Joyner-Boore distance (Bindi et al., 2011) and the shortest rupture distance (Cauzzi et al., 2015). To explore the impact of uncertainty of the M_{max} of each source in our estimation, the *UHS* for the M_{max} ± its standard deviation (1 *sD*, Table 3) have been calculated (Figure 6). Furthermore, to consider the random uncertainty linked to the standard deviation of each *GMPE*, we performed a number *n* of simulations of the scenario decided by the user, following a Monte Carlo-like approach. For this work, we performed 10,000 different simulations for each *GMPE*, for a total of 20,000 scenario simulations, and finally we calculated the average between the two relationships giving a weight of 0.5 to each relationship. Subsequently, we calculated the median and the confidence interval at 16% and 84% for the averaged 10,000 scenarios (Figure 6). For the finite element modelling, the two extremes have been selected for each source, i.e. the maximum and the minimum spectrum (Figure 6). In doing so, we consider the uncertainty in the magnitude, the uncertainty in the individual *GMPE* and the uncertainty related to the use of different *GMPE*s. Following this approach, we calculated the *UHS* for each seismogenic source (Figure 7); the differences between them depend mainly on the different M_{max} and the different distance from Cola cave.

4.4 Numerical modelling

Because a speleothem can be considered as a cantilever beam, with height *H* and diameter *D* (e.g. Cadorin et al., 2001; Mendecki and Szczygieł, 2019; Figure 5), we performed a numerical modelling to study its behaviour during the passage of the seismic waves, based on its natural frequency of vibration. We used a *FEM* modelling approach taking advantage of the *SAP2000* software (*www.csiamerica.com/products/sap2000*), which uses geometric, physical, and mechanical properties to compute the response of speleothems to the ground motion. This method is a numerical technique designed to approximate a problem described by partial differential equations, making the solution of the problem a system of algebraic equations. By this method, the macroscopic system is subdivided into small elements (Figure 5), and then the contribution of each element is cumulated to study the overall behaviour. To perform the *FEM* modelling with the *SAP2000* software, it is necessary to know the geometric (*H*, *D*), physical and mechanical (ρ, *Ed,* σ_T) parameters of the speleothems.

The geometric parameters were collected during the cave survey and are described in paragraph 5.1. The collected samples were analysed at the geotechnical laboratory of *DICEA* (*Department of Civil, Architectural and Environmental Engineering - Federico II University of Naples*) to evaluate physical and mechanical properties. Specifically, density values ρ of irregularly shaped samples were obtained by using the water displacement method, while mechanical parameters (compressive strength σ, dynamic young modulus *Ed)* were derived from uniaxial compressive load-deformation tests (Table 4) (see also Colella et

al., 2017). Furthermore, the tensile strength (σ_T) has been obtained empirically according to literature data that indicate values between 5% and 10% for the unconfined compressive strength (Hoek & Brown, 1997; Nazir et al., 2013; Trivedi, 2013; Perras & Diederichs, 2014). Specifically, we evaluated the threshold values as the minimum tensile strength that must be reached to break the speleothems (dotted lines in Figures 10 and 11). We used the minimum measured value of unconfined compressive strength (7.35 MPa) and so the thresholds range from 0.365 to 0.735 MPa. It should be noted that measured values of density ρ, dynamic young modulus *Ed* and tensile strength σ_T agree well with previous studies conducted on speleothems (stalactites, stalagmites, pillars or soda straw) from different caves and contexts (Gribovszki et al., 2008, 2013, 2018; Cadorin et al., 2001; Lacave et al., 2000, 2003, 2004; Szeidovitz et al., 2008; Gilli et al., 1999).

After the geometric and mechanical parameters are defined, the first step in this method is the discretization of the whole system into finite elements, called nodes and beams (Figure 5). Once the beam element with height *H* is created, this element is divided into n elements of smaller dimensions that are connected by nodes. Then, we assigned to each element a circular section, with diameter *D* and a constant value of ρ *and Ed*. In this work, the speleothems were considered without variations in mechanical parameters (ρ and *Ed*) and diameter along their axis, but we explored the uncertainty in the ρ evaluation, using the two limit values in the calculations (1.93-2.35 g/cm^3). In the same way, we explored the impact of the uncertainty in the dynamic young modulus *Ed* value, which, unlike ρ, can be considered neglectable in the modelling. The last step in the *FEM* analysis is the selection of the earthquake ground acceleration; the software allows the user to select different seismic input among which the response-spectrum to be used in the modelling. In this work, we used the *UHS* obtained following the seismic hazard analysis described before.

Because of the variable geometry of stalagmite COLA-3 along its axis, two types of modelling were carried out, called "simple" and "complex", respectively. In the former scenario, the diameter size does not vary along the axis of the speleothem, whose geometry is cylindrical. In the latter model the diameter size varies along the axis in a way that best approximates the actual geometry (Figure 5). This second modelling allowed to highlight the critical section of the stalagmite, such as the base and the tip, which results in a very different behaviour relative to the simple modelling. The same geometric and mechanical parameters were used in both simple and complex modelling, except for the speleothem diameter. In the first case the diameter is equal to 0.34 cm and in the second case it varies along the axis of the speleothem (Figure 5). Once all input parameters are set, the software provides, for a given direction of acceleration, the maximum displacements, forces (and their moments *M*), and stresses for each of the vibration mode of the speleothem. Using the moment (*M*) in the following equation:

$$\sigma = M\, r / I \qquad \text{(eq. 1)}$$

where r is the radius of the speleothem, *I* is the moment of inertia (*I=(r^4*π)/4*) of the circumferential transversal speleothem section of radius r, it is possible to calculate the failure tensile stress (σ) due to the selected earthquake ground acceleration. In an analytical approach, the acceleration value is obtained from eq. 1 so to reach the tensile stress value beyond which the speleothem breaks. In our approach instead, we do not have to calculate the acceleration value as it is one of our input data. We instead compare the changes in tensile stress data obtained through modelling (two values exploring the density uncertainty, dashed and solid lines in Figures 10 and 11) with the tensile strength thresholds obtained from laboratory tests (dotted lines in Figures 10 and 11). Accordingly, we can establish whether a given seismic input, and therefore the seismogenic source associated with it, is able or not to cause the collapse of the studied speleothem, and in the former case where the critical section of the speleothem occurs.

5. Results

5.1 Age of speleoseismic events

The total number of collected samples is nine, from four different sites. The U/Th and ^{14}C dating (Tables 1 and 2) provide constraints on the age of speleoseismic events (Table 5, Figure 8).

Four samples provide information from room *F* in the inner part of the southwestern branch of the cave (Figure 2). COLA-20 and COLA-21 are two small (~10 cm length) stalactites fallen toward the SSE and partly cemented on the floor (Figures 2, 4a). Nearby TRAP-2 come from the youngest (pre-event) layer of a fallen stalagmite, whereas TRAP-1 is the oldest (post-event) layer of a younger stalagmite (~2 cm long) grown upon the former (Figures 2, 4d). The ages of the samples TRAP-1 and TRAP-2 outline an event between ~8.0-1.5 ka (Table 5). Samples COLA-20 and COLA-21 collapsed after ~8.0 and ~1.1 ka, respectively. Whereas fall of COLA-20 was likely coeval to breakage of TRAP-2, collapse of COLA-21 occurred during a younger event.

In room *D* on the northeast branch of the cave, sample COLA-3 comes from the pre-event layer of the stalagmite chosen for modelling and samples COLA-1 and COLA-2 were extracted from the post-event layer of two small stalagmites (~10 cm length) grown above the stump left by the collapsed stalagmite (Figures 2, 4b-c). Sample COLA-4 was extracted from the oldest (post-event) layer of a stalagmite grown above an undated fallen speleothem nearby speleothem COLA-3. Samples COLA-3 (pre-event) and COLA-1 and COLA-2 (post-event) constrain a speleoseismic event whose age broadly spans between ~7-14 and ~4-5 ka (Table 5, Figure 8). The age bracket for this event is rather uncertain. Sample COLA-3 shows a high detrital contamination, as indicated by ^{232}Th (Table 1), and its corrected age strongly depends on the chosen initial $^{230}Th/^{232}Th$ activity ratio. For example, if a value of 2.96±0.1 were applied, as in Ferranti et al.

(2019), the ^{230}Th-corrected age would be 4.3 ka. This is not the case for the other speleothem samples that show a very small detrital thorium component. The post-event age bracket is more tightly constrained. Although COLA-1 and COLA-2 have ages median probability that differ of ~1 ka, they could have started growing within few hundred years from each other in the uncertainty range. Sample COLA-4 age documents a speleoseismic event older than ~3.5 ka, which could coincide with the event that caused collapse of COLA-3 within the same room (Table 5, Figures 2, 8).

Finally, in room *E* (east branch of Cola cave), we sampled the base of a stalagmite (CRLL ~6 cm long) grown upon a large limestone block fallen from the vault of the cave (Figures 2, 4e). The U/Th age of sample CRLL implies that the block fell from the ceiling prior to ~12.5 ka (Table 5, Figure 8).

5.2 Evaluation of amplification phenomena from noise measurement

Figure 9 shows the *H/V* ratios obtained at each station, for clarity of the figure we show the *H/V* mean curve and standard deviations computed for each measurement site. Figure 9 also reports the results of directional noise analysis and the mean *FAS* computed for the three different components (Z in blue, NS in green and EW in red) for each station. The *H/V* curves show a good agreement in terms of shape within the three stations. Two peaks are observed at frequency of about 1.5 Hz and 2.4 Hz in all sites. In all the three cases, the observed *H/V* peaks are due to signal characterized by energy higher on the horizontal's components compared to the vertical one, as clearly indicated by the *FAS* (Figure 9). Moreover, a clear polarization in the north and south directions is observed for the *H/V* peaks around the picks. Finally, also the amplitudes of *H/V* peaks (mean values) are comparable within the three stations with values close to 2 or slightly less than 2 for the peaks at 1.5 Hz and of about 1.7÷1.8 for the higher frequency peaks. A further spectral peak around 15-20 Hz is present in only one measurement (COL1). Also, in this latter case, this peak is characterized by an amplitude value (of about 1.5) significantly lower than the threshold used to identify local seismic amplification effects from HV spectral ratios analysis.

Summing up, the *H/V* curves at the sites show similar characteristics both in terms of fundamental frequencies and spectral shapes, the weak peaks observed (with amplitudes ≤ 2) suggest no important amplification phenomena (SESAME criteria and guidelines, Bard et al., 2005). Based on these results, we have not used the site contribution in theoretical spectral response simulated at the cave bedrock.

5.3 Numerical modelling

The numerical modelling results, obtained with both the "simple" and "complex" models, show how the value of the tensile stress (σ_T) arising from seismic motion varies along the speleothem axis (Figures 10 and 11). In the "simple" modelling (Figure 10) the maximum values of σ_T are at the base of the

speleothem, and as we move upward the values decrease until they are null at the top. For three out of the five seismogenic sources for which seismic input was calculated, the minimum threshold value of tensile strength was not reached. This therefore means that a possible earthquake generated by seismogenic sources *"Salto Valley"*, *"Campo Felice-Ovindoli"* and *"Velino"* is not able to cause the collapse of the speleothem when a "simple" geometry is adopted. The "simple" modelling allowed us to make a skimming between the possible sources that caused collapse of COLA-3 and, based on results, we discarded the latter three sources in "complex" modelling.

In Figure 11 we compare the variations of the tensile stress values σ_T along the speleothem axis with the threshold values of tensile strength for the "complex" modelling using the input *UHS* obtained for the *"Fucino"* and *"Liri"* seismogenic sources. In this scenario, the maximum value of σ_T is not at the base of the speleothem, but it increases from the base to a maximum point beyond which it decreases until zero at the top. This result is in excellent agreement with the geometric data of the modelled speleothem. Indeed, the maximum tensions that led to the speleothem breakage occurred at the exact point where the speleothem has a narrowing of its axis, which therefore represents a vulnerable section. This maximum value of σ_T was produced at ~22 cm height, which perfectly matches the elevation of the stump left by the breakage (Figure 5). Results of the complex modelling show that only the seismogenic source *"Liri"* reaches the minimum threshold value of tensile strength, suggesting it is the most likely source of the earthquake recorded by the collapse of speleothem COLA-3.

6. Discussion

Taken together, ages from pre- and post-event layers define three distinct speleoseismic events: the pre-penultimate with an age >12.5 ka, the penultimate between ~7-14 and ~4-5 ka, and the ultimate after 1.1 ka (Table 5). We relate these events to paleo-earthquakes that caused significant ground motion and collapses of cave speleothems. Unfortunately, pre- and post-event layers are only available for two speleothem couplets (COLA-3/COLA-1&2 and TRAP-1/TRAP-2) and refer to the penultimate event (or for the ultimate event for the latter couple). For the remaining events, either pre- or post-event ages are only defined (Table 5). In addition, a large time span separates pre- and post-event layers for the two speleothem couplets, impacting a tight definition of the age of the penultimate and possibly the ultimate events.

We can mitigate the above uncertainties and better refine the paleo-earthquake age estimate based on the acceptable assumption that growth of post-event stalagmites occurred soon after the collapse of the speleothem upon which they grew. We do not consider in this approach sampling and measurement errors that are too small to match the large time gap observed.

For the penultimate event, although a significant time span is observed between pre- and post-

456 event layers, the simplest interpretation is that the circulation-precipitation system closed long before the
457 event and was re-opened by seismic shaking. We refer to this assumption as the post-event growth
458 hypothesis. We are aware that closure and opening of the system could arise from changes in climatic and
459 hydrologic conditions as well. However, we do not expect significant variations in the limited time span
460 studied here when the Holocene climatic optimum was attained (Rossignol-Strick, 1999; Giraudi et al.,
461 2011). The hypothesis is corroborated by the observation that, when more than one single age
462 determination is available for post-event layers as in the case of COLA-1, COLA-2 and COLA-4 from room D,
463 their value overlap or is very close. These ages may indicate a sudden opening of the circulation-
464 precipitation system in the limestone above room D that in our view is related to seismic shaking during the
465 penultimate event. The inverse hypothesis, that shaking closed the system that was fortuitously opened
466 long after, seems untenable.
467 Bearing the above in mind, we suggest that the pre-penultimate event occurred at or slightly before
468 ~12.5 ka and is documented by a stalagmite (sample CRLL) grown on a large limestone block fallen from the
469 vault of the cave in room *E* (Figure 2). We compare this result with the paleoseismological data (trenches
470 and ^{36}Cl cosmogenic data; Galadini & Galli, 1999; Galli et al., 2008, 2012; Schlagenhauf et al., 2010, 2011;
471 Palumbo et al., 2004) available for the *"Fucino"* source (Figure 8). Cosmogenic data identified a possible
472 exhumation event older than 14.7±1 ka (Schlagenhauf et al., 2011) that could be the same identified in this
473 work. An alternative view, that we regard as more likely based on the post-event growth hypothesis
474 outlined above, is that the pre-penultimate event relates to a faulting event found around 12.5 ka in
475 paleoseismic trenches on the *"Fucino"* fault system (Galadini & Galli, 1999), which produced a significant
476 vertical displacement (~3 m on SBGM fault and 1-2 m on the Trasacco fault, a secondary splay of the
477 system).
478 Within the post-growth hypothesis, the maximum age of the penultimate event is suggested by the
479 oldest (COLA-1) post-event layer at 5.1 ka, which, within uncertainty, could be as young as 4.8 ka (Table 5).
480 Post-event layers COLA-2 (on the same stalagmite) and COLA-4 (on a nearby speleothem), with maximum
481 ages of 4.3 and 3.8 ka, respectively, probably started growing some hundred to a thousand years after the
482 fall. Comparison of our results for the penultimate event with the *"Fucino"* paleoseismological observations
483 available from literature (Figure 8) does not fit perfectly the exhumation event recorded by Schlagenhauf et
484 al. (2011) at 4.8 +0.3/-0.4 ka using ^{36}Cl data on the Magnola fault plane or the trench record by Galadini &
485 Galli (1999), where the closest event occurred between ˜6.0 and 5.6 ka.
486 Finally, the pre- and post-event layers TRAP-2 and TRAP-1 brackets the ultimate event at ~8.0-1.5
487 ka, and COLA-21 after 1.1 ka. Although the fall of TRAP-2 could have occurred during the penultimate
488 event, by considering the post-growth hypothesis, we regard this fall as constrained by the 1.55±0.07 ka
489 age of TRAP-1**.** In support of this, nearby stalactite COLA-21 (Figure 2) fell on the ground after 0.91-1.34 ka.
490 Considering uncertainties (Table 5), the two estimates may be separated by only 140 years, therefore they

491 are both assigned to the ultimate event.

492 The ultimate event can be compared to the trench rupture found between 426-782 CE on the
493 Fucino fault (Figure 8; Galli et al., 2008). These authors attributed the trench offset to the earthquakes that
494 hit Rome in 508 CE causing serious damages to the Coliseum (Galadini & Galli, 2001). The last ^{36}Cl
495 exhumation found on the Magnola fault plane (Schlagenhauf et al., 2010, 2011) has an age comparable to
496 the ultimate speleoseismic event as well. The Magnola fault represents the northern segment, closest to
497 the Cola cave, of the *"Fucino"* fault system. However, the damages occurred in the distant site of Rome
498 suggest that the entire ~38 km fault system ruptured contemporarily (Galli et al., 2012). In principle, we
499 cannot fully exclude that the ultimate speleoseismic event recorded in the cave occurred during the
500 devastating 1915 M_w 7 earthquake, the strongest recorded in central Italy (Rovida et al., 2016). This
501 earthquake was generated similarly by the entire *"Fucino"* fault system, with surface faulting recognized on
502 several segments (Oddone, 1915), and an inferred rupture directivity from the SE towards the NW (Berardi
503 et al., 1999).

504 For the penultimate event, we carried out a vulnerability analysis of COLA-3 to find a direct
505 attribution to a seismogenic source potentially responsible for the collapse. Using seismogenic source and
506 seismic hazard models, we calculated the expected ground motion (i.e. Uniform Hazard Spectra) in the cave
507 by the selected sources in turn, in a determinist approach, and compared it to the calculated failure tensile
508 stress (σ_T) of the stalagmite. The results suggest two possible seismogenic sources responsible of the
509 collapse: the *"Fucino"* and the *"Liri"* sources. The "complex" modelling, where the speleothem diameter
510 size varies along the axis, suggests *"Liri"* as the most likely source of the recorded shaking (see paragraph
511 5.3). It is important to highlight that we explored uncertainties related to the variability in density and
512 tensile strength, and the maximum expected magnitude and ground motion (i.e. Ground Motion Prediction
513 Equations), but several other sources of error remain unquantified. The results could be affected, for
514 example, by the rupture directivity, as happened for the 1915 earthquake, or by the actual hypocentre
515 location, hypothesized in our modelling at the bottom of the fault rupture and in the centre of the fault
516 system. Besides, we cannot exclude that changes in orientation of *C* axes of calcite crystals in the
517 speleothem, from horizontal at the base to vertical above, can create sections potentially prone to
518 breakage even in case of weaker ground motions. Finally, we cannot exclude the general variations of the
519 mechanical parameters, like for the example the density δ, inside the stalagmite, that we considered
520 homogeneous.

521 For these reasons, although the *"Liri"* fault remains the most likely source of the large paleo-
522 earthquakes recorded in the cave, and specifically of the penultimate event, we cannot exclude *"Fucino"* as
523 another potential source. This alternative scenario may be supported by the possible directivity of the
524 rupture towards NNW and a hypocentre closer to the Cola cave during the speleoseismic events studied
525 here. The *"Liri"* fault recent activity is debated and no paleoseismological data on the fault are available to

be compared to our event age. On the other hand, the abundance of paleoseismological data on the *"Fucino"* source renders the comparison possible, and we were able to match our speleoseismological data of two events (the ultimate and the pre-penultimate) with the paleoseismological record.

7. Conclusions

Our study allowed to reconstruct the speleoseismological history of the Cola cave in central Italy and to identify seismogenic sources potentially responsible for the collapse of a tall stalagmite and for two additional speleoseismic events.

Using the samples ages and the comparison with available paleoseismological data for active faults in the region surrounding the cave, we identified three speleoseismic events: the pre-penultimate occurred before but probably near ~12.5 ka, the penultimate occurred around ~5 ka, and the ultimate around ~1.5 ka and consistent with the 508 AD earthquake, which caused damages to the Coliseum in Rome.

The seismic hazard and vulnerability analysis of the tall stalagmite, collapsed during the penultimate event, allowed to find a direct attribution to a seismogenic source potentially responsible for the collapse. Modelling suggests the *"Liri"* fault as the most likely seismogenic source responsible for the ground shaking.

The *"Fucino"* fault system cannot be excluded as a potential source of collapsing in the cave. In support of this, the ages of two speleoseismic event matches some of the events found in trenches and on exhumed fault planes along the system.

We believe that the approach presented here can be useful to improve the paleoseismological data record available in active areas similar to the central Apennines, mainly collected using "classical" trench methods (e.g. Galli et al., 2008) or through more "innovative" investigations like fault surface exposure dating by cosmogenic technique (e.g. Benedetti & Van Der Woerd, 2014; Tesson et al., 2016).

The numerical FEM approach, using the best approximation of the complex speleothem geometry, allows to evaluate in detail the speleothem behavior during ground motion, and to precisely define the point of breakage as the weakest section of the speleothem.

The integrated use of seismic hazard and speleothem vulnerability analysis allowed to find a direct attribution of the penultimate speleoseismological event to a seismogenic source and suggested as possible the activity of the *"Liri"* fault, that should be considered more carefully into seismic hazard and risk models.

Further developments of the approach could integrate fault segmentation relaxation and the possible fault interactions into the seismic hazard model (e.g. Verdecchia et al., 2018; Visini et al., 2020; Valentini et al., 2020) and a better treatment of the uncertainties involved in the definition of the mechanical properties of broken speleothems and in the age record of speleoseismic events.

Acknowledgements

We sincerely thank S. Di Bianco, J. De Massis and P. Teodoro who helped sampling and collecting the cave data; F. Visini who helped us during the seismic noise measurements acquisition and discussed with us the seismic hazard results; D. Berardi who led us in the Cola cave; F. Rizzo who helped us during the initial part of FEM modelling; S. Agostini for useful discussions on speleoseismology and for providing his papers collection. Finally, we would like to thank the Editor T. Schildgen, the Associate Editor L. Dal Zilio and the two reviewers C.P. Rajendran and J. Szczygieł for helpful comments and revisions that significantly improved the manuscript. All the parametric data for sample dating, seismogenic sources and the speleothems physical and mechanical data are reported in tables (Tables 1-2-3-4) and have been taken from published literature, listed in the references. Data supporting the sample dating can be found also in the Pangaea repository at https://doi.pangaea.de/10.1594/PANGAEA.922154 and https://doi.pangaea.de/10.1594/PANGAEA.922156.

References

Bar-Matthews, M., Ayalon, A., Kaufman, A., & Wasserburg, G. J. (1999). The Eastern Mediterranean paleoclimate as a reflection of regional events: Soreq cave, Israel. *Earth and Planetary Science Letters, 166*(1-2), 85-95. https://doi.org/10.1016/S0012-821X(98)00275-1

Bard, P.-Y., SESAME-Team (2005). Report D23.12, Guidelines for the Implementation of the H/V Spectral Ratio Technique on Ambient Vibrations Measurements, Processing and Interpretation in European Commission: Research General Directorate, Project No. EVG1-CT-2000-00026. SESAME, p. 62 available online at: http://sesame-fp5.obs.ujf-grenoble.fr.

Becker, A., Davenport, C. A., Eichenberger, U., Gilli, E., Jeannin, P. Y., & Lacave, C. (2006). Speleoseismology: A critical perspective. *Journal of Seismology, 10*, 371-388. https://doi.org/10.1007/s10950-006-9017-z

Becker, A., Häuselmann, P., Eikenberg, J., & Gilli, E. (2012). Active tectonics and earthquake destructions in caves of northern and central Switzerland. *International Journal of Speleology,41*, 35-49. https://doi.org/10.5038/1827-806X.41.1.5

Benedetti, L. C., & Van Der Woerd, J. (2014). Cosmogenic nuclide dating of earthquakes, faults, and toppled blocks. *Elements, 10*(5), 357-361. https://doi.org/10.2113/gselements.10.5.357

Berardi, R., Contri, P., Galli, P., Mendez, A. & Pacor F. (1999). Modellazione degli effetti di amplificazione locale nelle città di Avezzano, Ortucchio e Sora. In: Castenetto S. and Galadini F. (eds), 13 gennaio del 1915. Il terremoto nella Marsica, Servizio Sismico Nazionale, pp. 349-372.

Bindi, D., Pacor, F., Luzi, L., Puglia, R., Massa, M., Ameri, G., & Paolucci, R. (2011). Ground motion prediction equations derived from the Italian strong motion database. *Bulletin of Earthquake Engineering, 9*, 1899-1920. https://doi.org/10.1007/s10518-011-9313-z

595 Boncio, P., Lavecchia, G., & Pace, B. (2004). Defining a model of 3D seismogenic sources for Seismic Hazard
596 Assessment applications: The case of central Apennines (Italy). *Journal of Seismology*, *8*(3), 407–425.
597 https://doi.org/10.1023/B:JOSE.0000038449.78801.05
598 Bonnefoy-Claudet, S., Cornou, C., Bard, P. Y., Cotton, F., Moczo, P., Kristek, J., et al. (2006). H/V ratio: a tool
599 for site effects evaluation. Results from 1-D noise simulations. *Geophysical Journal*
600 *International, 167,* 827–837.
601 Bosi, C. (1975). Osservazioni preliminari su faglie probabilmente attive nell'Appennino centrale. *Boll. Soc.*
602 *Geol. Ital*. 94 (1975) 827– 859.
603 Cadorin, J. F., Jongmans, D., Plumier, A., Camelbeeck, T., Delaby, S., & Quinif, Y. (2001). Modelling of
604 speleothems failure in the Hotton cave (Belgium). Is the failure earthquake induced? *Geologie En*
605 *Mijnbouw/Netherlands Journal of Geosciences, 80*(3-4), 315-321.
606 https://doi.org/10.1017/s001677460002391x
607 Cauzzi, C., Faccioli, E., Vanini, M., & Bianchini, A. (2015). Updated predictive equations for broadband
608 (0.01–10 s) horizontal response spectra and peak ground motions, based on a global dataset of digital
609 acceleration records. *Bulletin of Earthquake Engineering*, *13*(6), 1587–1612.
610 https://doi.org/10.1007/s10518-014-9685-y
611 Cheloni, D., De Novellis, V., Albano, M., Antonioli, A., Anzidei, M., Atzori, S., et al. (2017). Geodetic model of
612 the 2016 Central Italy earthquake sequence inferred from InSAR and GPS data. *Geophysical Research*
613 *Letters*, *44*(13), 6778–6787. https://doi.org/10.1002/2017GL073580
614 Chiaraluce, L., Valoroso, L., Piccinini, D., Di Stefano, R., & De Gori, P. (2011). The anatomy of the 2009
615 L'Aquila normal fault system (central Italy) imaged by high resolution foreshock and aftershock
616 locations. *Journal of Geophysical Research: Solid Earth*, *116*(12).
617 https://doi.org/10.1029/2011JB008352
618 Cinti, F. R., Pantosti, D., De Martini, P. M., Pucci, S., Civico, R., Pierdominici, S., et al. (2011). Evidence for
619 surface faulting events along the Paganica fault prior to the 6 April 2009 L'Aquila earthquake (central
620 Italy). *Journal of Geophysical Research: Solid Earth*, *116*(7). https://doi.org/10.1029/2010JB007988
621 Colella, A., Cremona, M., Di Bianco, S., Ferranti, L., Ramondini, M., & Calcaterra, D. (2017). Valutazione dei
622 principali parametri fisico- meccanici di alcuni speleotemi Italiani. In Atti III Convegno Regionale di
623 Speleologia «Campania Speleologica», 2-4 Giugno 2017, Napoli, Italy, pp. 101-112. ISBN 978-88-
624 89897-16-4.
625 Columbu, A., De Waele, J., Forti, P., Montagna, P., Picotti, V., Pons-Branchu, E., Hellstrom, J., Bajo, P., &
626 Drysdale, R. (2015). Gypsum caves as indicators of climate-driven incision and aggradation in a rapidly
627 uplifting region. *Geology, 43*, 539-542.

D'Agostino, N. (2014). Complete seismic release of tectonic strain and earthquake recurrence in the Apennines (Italy). *Geophysical Research Letters*, *41*(4), 1155–1162. https://doi.org/10.1002/2014GL059230

Devoti, R., Esposito, A., Pietrantonio, G., Pisani, A. R., & Riguzzi, F. (2011). Evidence of large scale deformation patterns from GPS data in the Italian subduction boundary. *Earth and Planetary Science Letters*, *311*(3–4), 230–241. https://doi.org/10.1016/j.epsl.2011.09.034

Di Domenica, A., & Pizzi, A. (2017). Defining a mid-Holocene earthquake through speleoseismological and independent data: Implications for the outer Central Apennines (Italy) seismotectonic framework. *Solid* Earth, 8, 161–176. https://doi.org/10.5194/se-8-161-2017

DISS Working Group (2015). Database of individual seismogenic sources (DISS), version 3.2.0: A compilation of potential sources for earthquakes larger than M 5.5 in Italy and surrounding areas. http://diss.rm.ingv.it/diss, Istituto Nazionale di Geofisica e Vulcanologia, doi: https://doi.org/10.6092/INGV.IT-DISS3.2.0

Faure Walker, J. (2014). Mechanics of continental extension from Quaternary strain fields in the Italian Apennines. *PhD Thesis*, pp 405.

Ferranti, L., Pace, B., Valentini, A., Montagna, P., Pons-Branchu, E., Tisnérat-Laborde, N., & Maschio, L. (2019). Speleoseismological constraints on ground shaking threshold and seismogenic sources in the Pollino range (Calabria, southern Italy). *Journal of Geophysical Research: Solid Earth, 124*(5), 5192-5216. https://doi.org/10.1029/2018JB017000

Forti, P., & Postpischl, D. (1980). Neotectonic data from stalagmites: sampling and analysis techniques. European Regional Conference on Speleology Sofia, CNR – Progetto Finalizzato Geodinamica, 351 Sofia, 2, 34-39.

Forti, P., Petrini, V., & Postpischl, D. (1981). Ricostruzione di fenomeni paleosismici da strutture carsiche. *Rendiconti Società Geologica Italiana*, *1981*(4),563-569.

Forti, P., & Postpischl, D. (1984). Seismotectonic and paleoseismic analyses using karst sediments. *Marine Geology, 55*(1-2), 145-161. https://doi.org/10.1016/0025-3227(84)90138-5

Forti, P. (2001). Seismotectonic and paleoseismic studies from speleothems: the state of the art. *Geologica Belgica, 4*(3-4), 175-185.

Galadini, F., & Galli, P. (1999). The Holocene paleoearthquakes on the 1915 Avezzano earthquake faults (central Italy): Implications for active tectonics in the central Apennines. *Tectonophysics, 308*(1-2), 143-170. https://doi.org/10.1016/S0040-1951(99)00091-8

Galadini, F., & Galli, P. (2000). Active tectonics in the central Apennines (Italy)–input data for seismic hazard assessment. *Natural Hazards*, *22*, 225–270.

661 Galadini, F., & Galli, P. (2001). Archaeoseismology in Italy: Case studies and implications on long-term
662 seismicity. *Journal of Earthquake Engineering, 5*(1), 35-68.
663 https://doi.org/10.1142/S1363246901000236
664 Galadini, F., Galli, P., & Giraudi, C. (1997). Geological investigations of Italian earthquakes: New
665 paleoseismological data from the Fucino Plain (Central Italy). *Journal of Geodynamics, 24*(1-4), 87-103.
666 https://doi.org/10.1016/s0264-3707(96)00034-8
667 Galadini, F., & Messina, P. (2001). Plio-quaternary changes of the normal fault architecture in the central
668 Apennines (Italy). *Geodinamica Acta, 14*(6), 321-344.
669 https://doi.org/10.1080/09853111.2001.10510727
670 Galadini, F., & Messina, P. (2004). Early-Middle Pleistocene eastward migration of the Abruzzi Apennine
671 (central Italy) extensional domain. *Journal of Geodynamics, 24*(1-4), 87-103.
672 https://doi.org/10.1016/j.jog.2003.10.002
673 Galli, P., Galadini, F., & Pantosti, D. (2008). Twenty years of paleoseismology in Italy. *Earth-Science Reviews*,
674 *88*(1–2), 89–117. https://doi.org/10.1016/j.earscirev.2008.01.001
675 Galli, P., Messina, P., Giaccio, B., Peronace, E., & Quadrio, B. (2012). Early Pleistocene to late Holocene
676 activity of the Magnola fault (Fucino fault system, central Italy). *Bollettino Di Geofisica Teorica Ed*
677 *Applicata*, *53*(4), 435–458. https://doi.org/10.4430/bgta0054
678 Gascoyne, M., Schwarcz, H. P., & Ford, D. C. (1980). A palaeotemperature record for the mid-Wisconsin in
679 Vancouver Island. *Nature, 285*, 474-476. https://doi.org/10.1038/285474a0
680 Gilli, E., Levret, A., Sollogoub, P., & Delange, P. (1999). Research on the February 18, 1996 earthquake in the
681 caves of Saint-Paul-de-Fenouillet area, (Eastern Pyrenees, France). *Geodinamica Acta, 12*(3-4), 143-
682 158. https://doi.org/10.1080/09853111.1999.11105338
683 Giraudi, C. (1988). Evoluzione geologica della Piana del Fucino (Abruzzo) negli ultimi 30.000 anni. *Il*
684 *Quaternario, 1*(2), 131-159.
685 Giraudi, C. (1992). Segnalazione di scarpate di faglia tardo-pleistoceniche sui Monti della Magnola
686 (Massiccio del Velino - Abruzzo). *Il Quaternario, 5*(1), 27-32.
687 Giraudi, C., Magny, M., Zanchetta, G., & Drysdale, R.N. (2011). The Holocene climatic evolution of
688 Mediterranean Italy: a review of the continental geological data. *The Holocene, 21*(1), 105-115.
689 Gribovszki, K., Paskaleva, I., Kostov, K., Varga, P., & Nikolov, G. (2008). Estimating an upper limit on
690 prehistoric peak ground acceleration using the parameters of intact speleothems in caves in
691 southwestern Bulgaria. In A. Zaicenco, I. Craifaleanu, I. Paskaleva (Eds.) Harmonization of seismic
692 hazard in Vrancea Zone with special emphasis on seismic risk reduction. NATO Science for peace and
693 security, series C: environmental security (pp. 287–308). Dordrecht: Springer. (ISBN: 978-1-4020-9241-
694 1).

695 Gribovszki, K., Bokelmann, G., Szeidovitz, G., Varga, P., Paskaleva, I., Brimich, L., & Kovacs., K. (2013).
696 Comprehensive investigation of intact, vulnerable stalagmites to estimate an upper limit on
697 prehistoric ground acceleration. In Proceedings of the Vienna congress on recent advanced in
698 earthquake engineering and structural dynamics & 13. D-A-CH Tagung, Vienna, Paper No. 445, p. 10.
699 Gribovszki, K., Esterhazy, S., & Bokelmann, G. (2018). Numerical Modeling of Stalagmite Vibrations. *Pure*
700 *and Applied Geophysics, 175*, 4501-4514. https://doi.org/10.1007/s00024-018-1952-4
701 Hellstrom, J. (2006). U-Th dating of speleothems with high initial ^{230}Th using stratigraphic constraint.
702 *Quaternary Geochronology, 1*(4), 289-295. doi:10.1016/j.quageo.2007.01.004
703 Hoek, E., & Brown, E. T. (1997). Practical estimates of rock mass strength. *International Journal of Rock*
704 *Mechanics and Mining Sciences, 34*(8), 1165-1186. https://doi.org/10.1016/S1365-1609(97)80069-X
705 Jaillet, S., Pons-Branchu, E., Maire, R., Hamelin, B., & Brulhet, J. (2006). Enregistrement de paléo-mises en
706 charge Holocènes dans deux stalagmites du réseau du rupt-du-puits (Barrois, France). Analyses
707 morphologiques des lamines et datations U/Th en TIMs. *Geologica Belgica*, *9*(3-4), 297–307.
708 Kagan, E. J., Agnon, A., Bar-Matthews, M., & Ayalon, A. (2005). Dating large infrequent earthquakes by
709 damaged cave deposits. *Geology, 33*(4), 261-264. https://doi.org/10.1130/G21193.1
710 Kagan, E.J., (2012). Multi-site Late Quaternary Paleoseismology in the Dead Sea Transform Region:
711 Independent Recording by Lake and Cave Sediments. Geological Survey of Israel report, GSI/17/2012.
712 Kagan, E. J., Cinti, F. R., Alfonsi, L., Civico, R., & Bar-Matthews, M. (2017). Broken speleothems reveal
713 Holocene and Late Pleistocene paleoearthquakes in Northern Calabria, Italy. *Quaternary International,*
714 *451*, 176-184. https://doi.org/10.1016/j.quaint.2016.10.023
715 Konno, K., & Ohmachi, T. (1998). Ground-motion characteristics estimated from spectral ratio between
716 horizontal and vertical components of microtremor. *Bulletin of the Seismological Society of America,*
717 *88*(1), 228-241.
718 Lacave, C., Levret, A., & Koller, M. (2000). Measurements of natural frequencies and damping of
719 speleothems. *Proc. of the 12th World Conference on Earthquake Engineering*, Auckland, New-
720 Zealand, Paper 2118, 2000.
721 Lacave, C., Koller, M. W., Eichenberger, U., & Jeannin, P. Y. (2003). Prevention of speleothem rupture during
722 nearby construction. *Environmental Geology, 43*, 892-900. https://doi.org/10.1007/s00254-002-0719-
723 4
724 Lacave, C., Koller, M. G., & Egozcue, J. J. (2004). What can be concluded about seismic history from broken
725 and unbroken speleothems? *Journal of Earthquake Engineering, 8*(3), 431-455.
726 https://doi.org/10.1080/13632460409350496
727 Lauritzen, S. E. (1995). High-Resolution Paleotemperature Proxy Record for the Last Interglaciation Based
728 on Norwegian Speleothems. *Quaternary Research, 43*(2), 133-146.
729 https://doi.org/10.1006/qres.1995.1015

Li, W. X., Lundberg, J., Dickin, A. P., Ford, D. C., Schwarcz, H. P., McNutt, R., & Williams, D. (1989). High-precision mass-spectrometric uranium-series dating of cave deposits and implications for palaeoclimate studies. *Nature, 339*, 534-536. https://doi.org/10.1038/339534a0

McDermott, F. (2004). Palaeo-climate reconstruction from stable isotope variations in speleothems: A review. In *Quaternary Science Reviews, 23*(7-8), 901-918. https://doi.org/10.1016/j.quascirev.2003.06.021

Mendecki, M., & Szczygieł, J. (2019). Physical constraints on speleothem deformations caused by earthquakes, seen from a new perspective: Implications for paleoseismology. *Journal of Structural Geology*, *126*, 146–155, doi:10.1016/j.jsg.2019.06.008.

Messina, P. (1996). Tettonica mesopleistocenica dei terrazzi nord-orientali del Fucino (Italia centrale). *Il Quaternario, 9*(1), 393-398.

Michetti, A. M., Brunamonte, F., Serva, L., & Vittori, E. (1996). Trench investigations of the 1915 Fucino earthquake fault scarps (Abruzzo, central Italy): Geological evidence of large historical events. *Journal of Geophysical Research: Solid Earth, 101(B3), 5921-5936.* https://doi.org/10.1029/95jb02852

Nazir, R., Momeni, E., Armaghani, D. J., & Amin, M. F. M. (2013). Correlation between unconfined compressive strength and indirect tensile strength of limestone rock samples. *Electronic Journal of Geotechnical Engineering, 18*, 1737-1746.

Oddone E., (1915). Gli elementi fisici del grande terremoto marsicano-fucense del 13 gennaio 1915. *Boll. Soc. Sism. It*., 19, 71-215.

Pace, B., Peruzza, L., Lavecchia, G., & Boncio, P. (2006). Layered seismogenic source model and probabilistic seismic-hazard analyses in central Italy. *Bulletin of the Seismological Society of America*, *96*(1), 107–132. https://doi.org/10.1785/0120040231

Pace, B., Boncio, P., Brozzetti, F., Lavecchia, G., & Visini, F. (2008). From regional seismic hazard to “scenario earthquakes” for seismic microzoning: A new methodological tool for the Celano Project. *Soil Dynamics and Earthquake Engineering*, *28*(10–11), 866–874. https://doi.org/10.1016/j.soildyn.2007.11.001

Pace, B., Peruzza, L., & Visini, F. (2010). LASSCI2009.2: Layered earthquake rupture forecast model for central Italy, submitted to the CSEP project. *Annals of Geophysics*, *53*(3), 85–97. https://doi.org/10.4401/ag-4847

Pace, B., Bocchini, G. M., & Boncio, P. (2014). Do static stress changes of a moderate-magnitude earthquake significantly modify the regional seismic hazard? Hints from the L’Aquila 2009 normal-faulting earthquake (Mw 6.3, central Italy). *Terra Nova, 26*(6), 430-439. https://doi.org/10.1111/ter.12117

Pace, B., Visini, F., & Peruzza, L. (2016). *FiSH*: MATLAB Tools to Turn Fault Data into Seismic-Hazard Models. *Seismological Research Letters*, *87*(2A), 374–386. https://doi.org/10.1785/0220150189

764 Pagani, M., Monelli, D., Weatherill, G., Danciu, L., Crowley, H., Silva, V., et al. (2014). OpenQuake Engine: An
765 Open Hazard (and Risk) Software for the Global Earthquake Model. *Seismological Research Letters*,
766 *85*(3), 692–702. https://doi.org/10.1785/0220130087
767 Palumbo, L., Benedetti, L., Bourlès, D., Cinque, A., & Finkel, R. (2004). Slip history of the Magnola fault
768 (Apennines, Central Italy) from 36Cl surface exposure dating: Evidence for strong earthquakes over
769 the Holocene. *Earth and Planetary Science Letters, 225*(1-2), 163-176.
770 https://doi.org/10.1016/j.epsl.2004.06.012
771 Pantosti, D., D'Addezio, G., & Cinti, F. R. (1996). Paleoseismicity of the Ovindoli-Pezza fault, central
772 Apennines, Italy: A history including a large, previously unrecorded earthquake in the Middle Ages
773 (860-1300 A.D.). *Journal of Geophysical Research: Solid Earth, 101*(B3), 5937-5959.
774 https://doi.org/10.1029/95jb03213
775 Papanikolaou, I. D., Roberts, G. P., & Michetti, A. M. (2005). Fault scarps and deformation rates in Lazio-
776 Abruzzo, Central Italy: Comparison between geological fault slip-rate and GPS data. *Tectonophysics,*
777 *408*(1-4), 147-176. https://doi.org/10.1016/j.tecto.2005.05.043
778 Perras, M. A., & Diederichs, M. S. (2014). A Review of the Tensile Strength of Rock: Concepts and Testing.
779 *Geotechnical and Geological Engineering, 32*, 525-546. https://doi.org/10.1007/s10706-014-9732-0
780 Peruzza, L., & Pace, B. (2002). Sensitivity analysis for seismic source characteristics to probabilistic seismic
781 hazard assessment in central Apennines (Abruzzo area). *Bollettino di Geofisica Teorica ed Applicata*,
782 *43*(1–2), 79–100.
783 Peruzza, L., Pace, B., & Visini, F. (2011). Fault-based earthquake rupture forecast in Central Italy: Remarks
784 after the L'Aquila Mw 6.3 Event. *Bulletin of the Seismological Society of America, 101*, 404-412.
785 https://doi.org/10.1785/0120090276
786 Pons-Branchu, E., Douville, E., Roy-Barman, M., Dumont, E., Branchu, P., Thil, F., Frank, N., Bordier, L., &
787 Borst, W. (2014). A geochemical perspective on Parisian urban history based on U-Th dating, laminae
788 counting and yttrium and REE concentrations of recent carbonates in underground aqueducts:
789 *Quaternary Geochronology*, *24*, 44–53. doi:10.1016/j.quageo .2014 .08.001.
790 Postpischl, D., Agostini, S., Forti, P., & Quinif, Y. (1991). Palaeoseismicity from karst sediments: the 'Grotta
791 del Cervo' cave case study (Central Italy). *Tectonophysics, 193*, 33-44.
792 Rajendran, C.P., Sanwal, J., Morell, K., Sandiford, M., Kotlia, R.S., Hellstrom, J. & Rajendran, K. (2016).
793 Stalagmite growth perturbations from the Kumaun Himalaya as potential earthquake recorders.
794 *Journal of Seismology*, 20, 579-594.
795 Reimer, P. J., Bard, E., Bayliss, A., Beck, J. W., Blackwell, P. G., Ramsey, C. B., et al. (2013). IntCal13 and
796 Marine13 radiocarbon age calibration curves 0–50,000 years cal BP. Radiocarbon, 55(4), 1869–1887.
797 https://doi.org/10.2458/azu_js_rc.55.16947.Roberts, G. P., & Michetti, A. M. (2004). Spatial and
798 temporal variations in growth rates along active normal fault systems: An example from The Lazio-

Abruzzo Apennines, central Italy. *Journal of Structural Geology*, *26*(2), 339–376. https://doi.org/10.1016/S0191-8141(03)00103-2

Roberts, G. P., & Michetti, A. M. (2004). Spatial and temporal variations in growth rates along active normal fault systems: An example from the Lazio-Abruzzo Apennines, central Italy. *Journal of Structural Geology, 26*(2), 339–376. https://doi.org/10.1016/S0191-8141(03)00103-2

Rossignol-Strick, M. (1999). The Holocene climatic optimum and pollen records of sapropel 1 in the eastern Mediterranean, 9000-6000 BP. *Quaternary Science Review, 4-5*, 515-530.

Rovida, A., Locati, M., Camassi, R., Lolli, B., & Gasperini, P. (2016). CPTI15, the 2015 version of the parametric catalogue of Italian earthquakes. Istituto Nazionale di Geofisica e Vulcanologia. https://doi.org/10.6092/INGV.IT-CPTI15

Rovida, A., Locati, M., Camassi, R., Lolli, B., & Gasperini, P. (2020). The Italian earthquake catalogue CPTI15. *Bulletin of Earthquake Engineering, 18*, 2953-2984. https://doi.org/10.1007/s10518-020-00818-y

Salvi, S., Cinti, F. R., Colini, L., D'Addezio, G., Doumaz, F., & Pettinelli, E. (2003). Investigation of the active Celano-L'Aquila fault system, Abruzzi (central Apennines, Italy) with combined ground-penetrating radar and palaeoseismic trenching. *Geophysical Journal International*, *155*(3), 805–818. https://doi.org/10.1111/j.1365-246X.2003.02078.x

Schlagenhauf, A., Gaudemer, Y., Benedetti, L., Manighetti, I., Palumbo, L., Schimmelpfennig, I., et al. (2010). Using in situ Chlorine-36 cosmonuclide to recover past earthquake histories on limestone normal fault scarps: A reappraisal of methodology and interpretations. *Geophysical Journal International, 182*(1), 36-72. https://doi.org/10.1111/j.1365-246X.2010.04622.x

Schlagenhauf, A., Manighetti, I., Benedetti, L., Gaudemer, Y., Finkel, R., Malavieille, J., & Pou, K. (2011). Earthquake supercycles in Central Italy, inferred from 36Cl exposure dating. *Earth and Planetary Science Letters*, *307*(3–4), 487–500. https://doi.org/10.1016/j.epsl.2011.05.022

Scotti, O., Visini, F., Benedetti, L., Boncio, P., Faure Walker, J., Pace, B., Peruzza, L., & Roberts, G. (2020). On the importance of fault modelling for seismic risk estimate. EGU2020-19434, https://doi.org/10.5194/egusphere-egu2020-19434

Serva, L., Blumetti, A. M., & Michetti, A. M. (1986). Gli effetti sul terreno del terremoto del Fucino (13 Gennaio 1915); tentative di interpretazione della evoluzione tettonica recente di alcune strutture. *Mem. Soc. Geol. It*., 35, 893-907.

Stuiver, M., Reimer, P.J., & Reimer, R.W. (2020). CALIB 7.1 [WWW program] at http://calib.org, accessed 2020-7-26.

Szeidovitz, G., Paskaleva, I., Gribovszki, K., Kostov, K., Surány, G., Varga, P., & Nikolov, G. (2008). Estimation of an upper limit on prehistoric peak ground acceleration using the parameters of intact speleothems in caves situated at the western part of Balkan Mountain Range, North-West Bulgaria. *Acta*

Geodaetica et Geophysica Hungarica, 43(2-3), 249-266. https://doi.org/10.1556/AGeod.43.2008.2-3.13

Talma, A. S., & Vogel, J. C. (1992). Late Quaternary paleotemperatures derived from a speleothem from Cango Caves, Cape Province, South Africa. *Quaternary Research, 37*(2), 203-213. https://doi.org/10.1016/0033-5894(92)90082-T

Tesson, J., Pace, B., Benedetti, L., Visini, F., Delli Rocioli, M., Arnold, M., et al. (2016). Seismic slip history of the Pizzalto fault (central Apennines, Italy) using in situ-produced 36Cl cosmic ray exposure dating and rare earth element concentrations. *Journal of Geophysical Research: Solid Earth, 121*(3), 1983-2003. https://doi.org/10.1002/2015JB012565

Trivedi, A. (2013). Estimating in Situ deformation of rock masses using a hardening parameter and RQD. *International Journal of Geomechanics, 13*(4). https://doi.org/10.1061/(ASCE)GM.1943-5622.0000215

Valentini, A., Visini, F., & Pace, B. (2017). Integrating faults and past earthquakes into a probabilistic seismic hazard model for peninsular Italy. *Natural Hazards and Earth System Sciences*, *17*(11), 2017–2039. https://doi.org/10.5194/nhess-17-2017-2017

Valentini, A., Pace, B., Boncio, P., Visini, F., Pagliaroli, A., & Pergalani, F. (2019). Definition of Seismic Input From Fault-Based PSHA: Remarks After the 2016 Central Italy Earthquake Sequence. *Tectonics*, *38*(2). https://doi.org/10.1029/2018TC005086

Valentini, A., Duross, C. B., Field, E. H., Gold, R. D., Briggs, R. W., Visini, F., & Pace, B. (2020). Relaxing segmentation on the Wasatch fault zone: Impact on seismic hazard. *Bulletin of the Seismological Society of America, 110*(1), 83-109. https://doi.org/10.1785/0120190088

Verdecchia, A., Pace, B., Visini, F., Scotti, O., Peruzza, L., & Benedetti, L. (2018). The Role of Viscoelastic Stress Transfer in Long-Term Earthquake Cascades: Insights After the Central Italy 2016–2017 Seismic Sequence. *Tectonics, 37*(10), 3411-3428. https://doi.org/10.1029/2018TC005110

Visini, F., Valentini, A., Chartier, T., Scotti, O., & Pace, B. (2020). Computational tools for relaxing the fault segmentation in probabilistic seismic hazard modelling in complex fault systems. *Pure Applied Geophysics*, *177*(5), 1855–1877.

Wathelet, M., Chatelain, J.-L., Cornou, C., Di Giulio, G., Guillier, B., Ohrnberger, M., & Savvaidis, A. (2020). Geopsy: A User-Friendly Open-Source Tool Set for Ambient Vibration Processing. *Seismological Research Letters, 91*(3), 1878-1889. doi:10.1785/0220190360.

Figures and Tables captions

Figure 1 - Tectonic sketch of the studied area. The star represents the Cola cave (coordinates in the box); the black circles represents the epicenters of the historical earthquakes reported in the CPTI15 catalogue (Rovida et al., 2016); the black lines are the major active faults outcropping in the area (in red the active faults modelled in this work). The numbers represent the modelled seismogenic sources: 1: *"Campo Felice-Ovindoli"*; 2: *"Fucino"*; 3: *"Salto Valley"*; 4: *"Velino"*; 5: *"Liri"*. *MF*: Magnola fault; *MHP*: Marsicano Highway-Parasano fault; *SBGM*: San Benedetto-Gioia dei Marsi fault. The hillshade has been produced from a DEM available at: http://www.sinanet.isprambiente.it/it/sia-ispra/download-mais/dem20/view.

Figure 2 – Map of the Cola Cave (modified from a map kindly provided by Daniele Berardi) showing the falling azimuth of broken stalagmites (arrows in map gives the trend; rose diagram distribution in inset provides the direction), the location and labels of dated samples and the seismic noise measurement sites (stars).

Figure 3 – Conceptual model showing the process of seismic breaking of the speleothems. a) An earthquake occurs in the vicinity of the cave and the speleothems oscillate due to the passage of the seismic waves. b) The speleothem oscillate due to the ground motion until its failure tensile stress is overcome and the speleothem breaks in the weakest part, often where the C axes of calcite crystals could change in orientation from horizontal at the base to vertical above. The speleothems fall down oriented with the mean direction of the seismic waves. c) After the collapse, new speleothems grow on top of the base and the fallen part of the broken speleothem. Dating the tip of the fallen part (A) and the base of the new speleothems (B) help to constrain the age of the collapse. d) If the speleothem is not vulnerable enough, instead of collapsing, it could change its growth axis. In this case the evidences of earthquakes are in the inner structure of it.

Figure 4 – Speleothem from the Cola cave: (a) site of the two fallen stalactites COLA-20 and COLA-21: in the two small pictures the sample COLA-20 in details, before the cut (on the right) and after the cut (on the left), in red the sampled layer; (b) site of TRAP-1 and TRAP-2 samples: TRAP-1 is the younger stalagmite grown upon the fallen stalagmite TRAP-1; in the small picture the sample TRAP-1 in details after the cut, in red the sampled youngest layer; (c) COLA-3 site: COLA-1 and COLA-2 are the two small stalagmites grown above the stump left by the collapsed stalagmite COLA-3; in the small picture a detail of the sample COLA-2 after the cut, with the arrow the sampled oldest layer; (d) CRLL sample site: CRLL is a small stalagmite grown upon a large limestone block fallen from the vault of the cave; in the two small pictures the sample CRLL in details, before the cut (on the right) and after the cut (on the left), in red the sampled layer.

Figure 5 – Sketch of the real geometry of COLA-3 and of its approximation in the simple and complex modeling. The dashed red line in the real case is the failure section, where COLA-3 broke after the earthquake. The 0.34 meters average section (D) is the section used for the simple modeling and for the central part of the complex modeling. The black dots in the simple and complex modeling are the nodes of the finite elements, which are connected by a beam. The difference between simple and complex shape are at the base and at the tip, where the complex model tries to approximate the real shape of COLA-3.

Figure 6 – An example of the uniform hazard spectra computed for a given source and the logic tree used to explore the epistemic uncertainty. For each seismogenic source, we computed the $M_{max} - sD$ and the $M_{max} + sD$. Then, for each moment magnitude, we run 10,000 different simulations for the two GMPEs and averaged them giving a weight of 0.5 to each relationship. Finally, we computed for the 10,000 averaged simulations, the median, and the confidence interval at 16% and 84%. At the end, for the modeling simulations and for each seismogenic source, we picked out the two UHS extremes (dashed/bold curves).

Figure 7 – Deterministic UHS, for each seismogenic source, used in the finite element modeling. For each source, we selected two UHS as described in section 4.3.

Figure 8 – Chronological scheme of the speleoseismic events recorded in Cola cave by crossing individual events found in the cave. The different symbols indicate the different dating techniques and the thick bars indicate the age uncertainties (Table 1). The gray bands indicate events constrained by both pre-event and post-event layers (the darker grey indicate the most probable ages). Event bracketed with dotted line indicates uncertainty in the pre-event or post-event age. In the upper part we show, as comparison, the paleoseismological data (trench data from Galadini & Galli, 1999; Galli et al., 2008, 2012; and ^{36}Cl cosmogenic data from Schlagenhauf et al., 2010, 2011; Palumbo et al., 2004) available for the *"Fucino"* source; with the dotted circles we show the possible matching events.

Figure 9 – H/V spectral ratios for the three different sites in Cola cave. The panels on the right show the average values of the spectral ratios with the relative standard deviations. The figure in the middle panels show the results of H/V rotated in the horizontal plane, i.e., as a function of azimuth. In the right side, the averaged Fourier Amplitude Spectra (FAS) for the three components of motion (blue curve refers to the vertical component). Each panel shows the code associated to the corresponding seismic stations (top right).

Figure 10 – Results of the simple modeling for the five seismogenic sources. For each source, we computed the failure tensile strength (σ) along the speleothem axis for four different cases in order to explore the

epistemic uncertainty in the modeling parameters (UHS and the density ρ). The dotted horizontal lines are the maximum and minimum threshold value of the failure tensile strength, beyond which the speleothem could collapse.

Figure 11 – Results of the complex modeling for the two seismogenic sources that showed higher results in the simple modeling (Figure 10). Different from the simple modeling, here, the modeled failure tensile strength (σ) reaches the highest value at 0.2 meters, the same point where the speleothem is collapsed (Figure 5).

Table 1 – Uranium-series measurements of the speleothem samples from the Cola cave. The concentrations of ^{238}U and ^{232}Th were determined using the enriched ^{236}U and ^{229}Th isotopes, respectively. $\delta^{234}Um = \{[(^{234}U/^{238}U)_{sample}/(^{234}U/^{238}U)_{eq}] - 1\} \times 1000$, where $(^{234}U/^{238}U)$sample is the measured atomic ratio and $(^{234}U/^{238}U)_{eq}$ is the atomic ratio at secular equilibrium. *Corrected ages for detrital ^{230}Th fraction were calculated using an initial $^{230}Th/^{232}Th$ activity ratio of 1.25±0.62.

Table 2 – AMS ^{14}C ages of the speleothem samples from Cola cave. The "dead carbon portion" DCP-corrected ^{14}C ages were calculated based on two different values of dead carbon incorporated in the speleothem (5%, and 10%). The ^{14}C ages were converted to calendar year (calibrated age) using the IntCal13 calibration curve (Reimer et al., 2013). The mean preferred calibrated age is the average of the median probability calculated from the two DCP values. The 1σ range for the preferred calibrated age represents the largest age interval.

Table 3 – Geometric parameters and list of M_{max} and its standard deviation (*sD*) of the Seismogenic Sources. *Id* = Identification number, *L* = along strike length, *Dip* = the inclination angle of the fault plane.

Table 4 – Geometrical features, physical and mechanical parameters of the investigated speleothems: *H* = Height (in-site average value over the failure section), *D* = Diameter (in-site average value of the failure section), δ = density, *Ed* = dynamic young modulus, σ_T = tensile strength thresholds.

Table 5 – Age constraints on speleoseismic events from U-Th and ^{14}C dating results.

Figure 1.

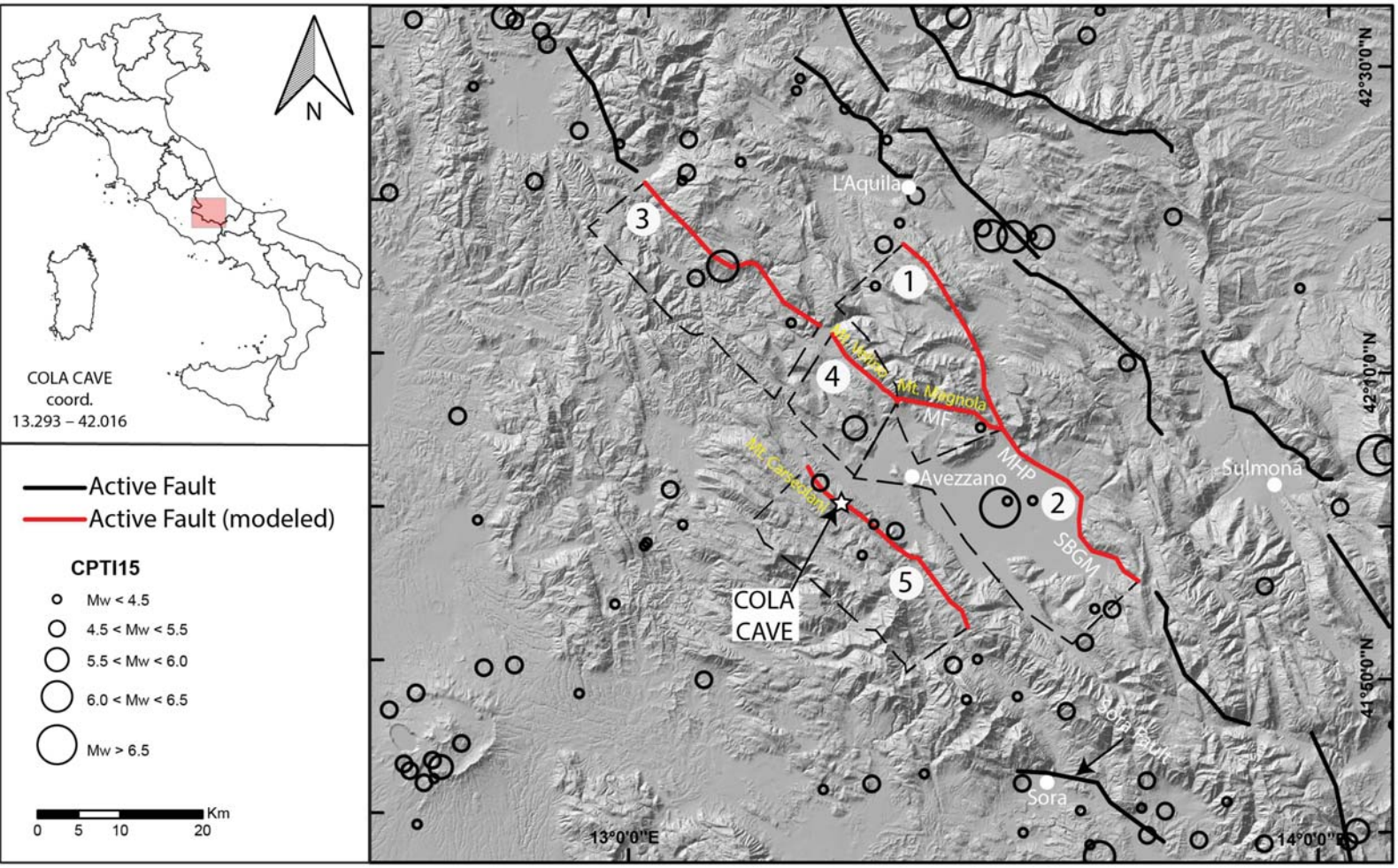
N
COLA CAVE
coord.
13.293 – 42.016
Active Fault
Active Fault (modeled)
CPTI15
Mw < 4.5
4.5 < Mw < 5.5
5.5 < Mw < 6.0
6.0 < Mw < 6.5
Mw > 6.5
Km
0 5 10 20
L'Aquila
Avezzano
Sulmona
Sora
Mt. Magnola
MF
MHP
SBGM
Mt. Carsoli
COLA CAVE
1
2
3
4
5
13°0'0"E
14°0'0"E
42°30'0"N
42°0'0"N
41°30'0"N

Figure 2.

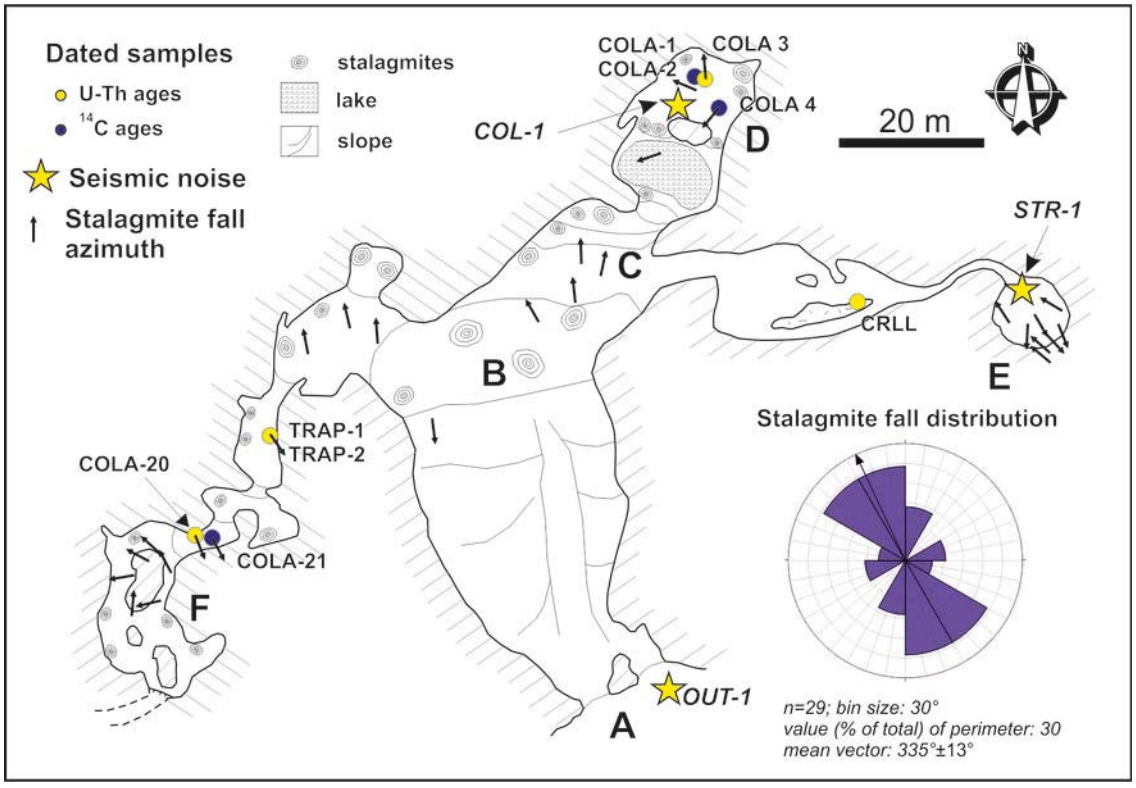
Dated samples
U-Th ages
14C ages
Seismic noise
Stalagmite fall azimuth
stalagmites
lake
slope
COLA-1
COLA-2
COLA 3
COLA 4
COL-1
D
20 m
N
STR-1
C
CRLL
B
E
TRAP-1
TRAP-2
COLA-20
COLA-21
F
OUT-1
A
Stalagmite fall distribution
n=29; bin size: 30°
value (% of total) of perimeter: 30
mean vector: 335°±13°

Figure 3.

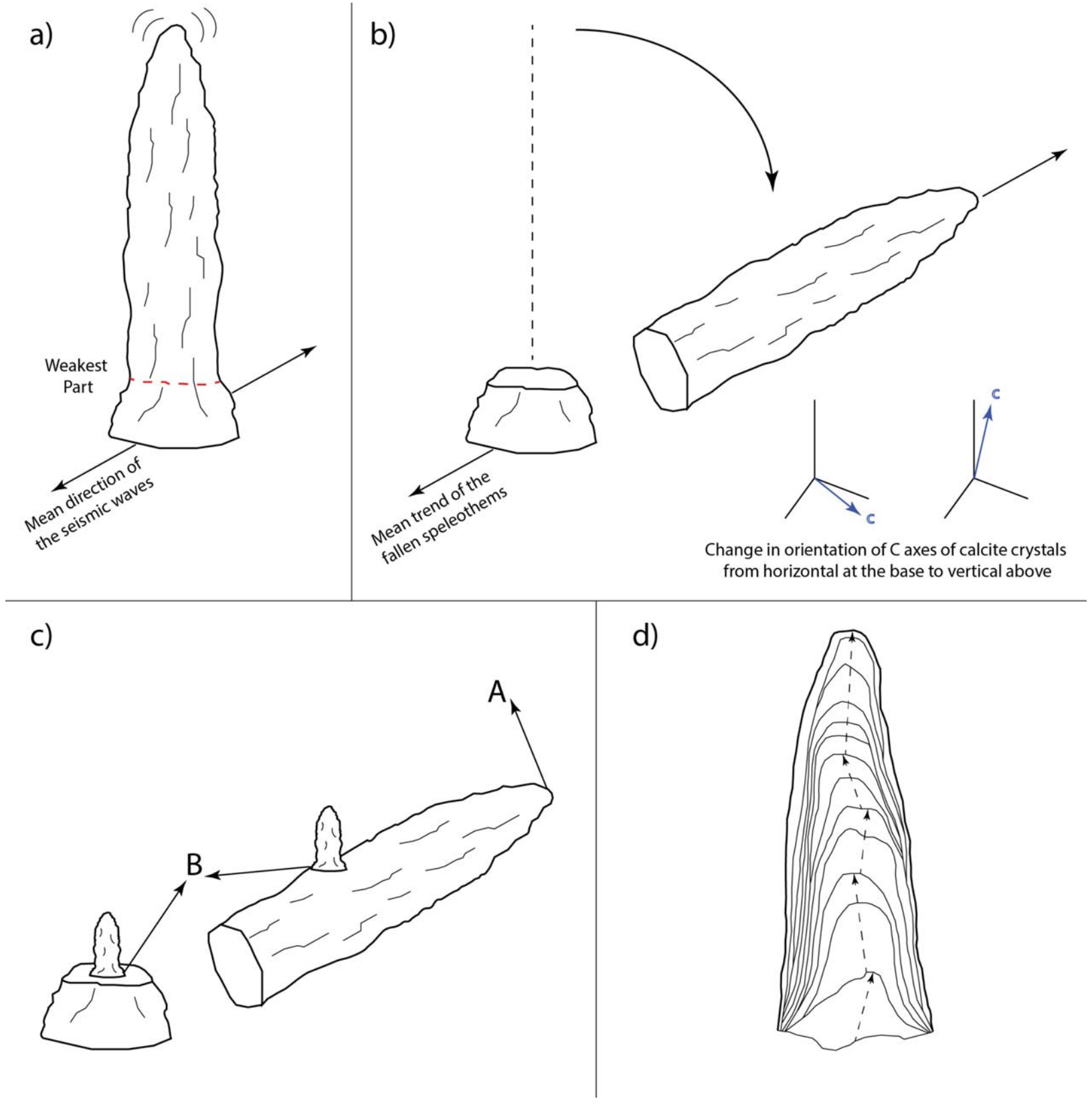
a)
Weakest
Part
Mean direction of
the seismic waves
b)
Mean trend of the
fallen speleothems
C
C
Change in orientation of C axes of calcite crystals
from horizontal at the base to vertical above
c)
A
B
d)

Figure 4.

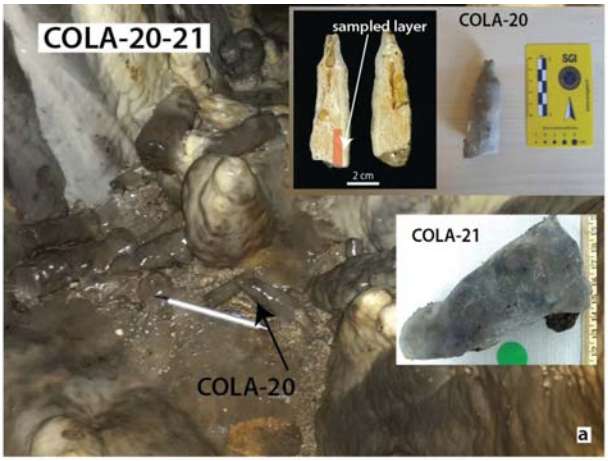
COLA-20-21
sampled layer
2 cm
COLA-20
COLA-21
COLA-20
a

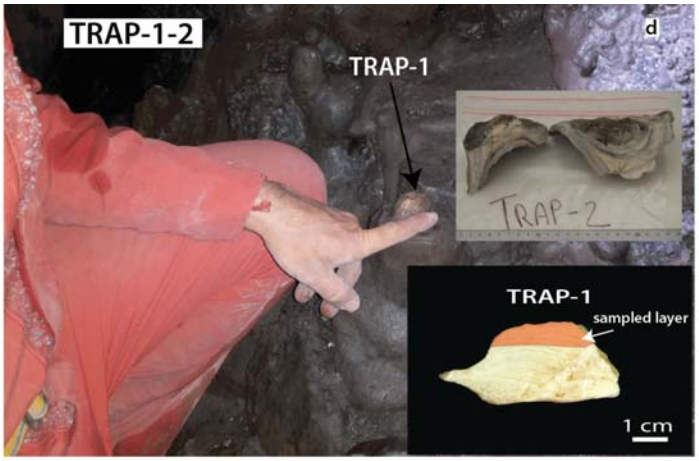
TRAP-1-2
d
TRAP-1
TRAP-2
TRAP-1
sampled layer
1 cm

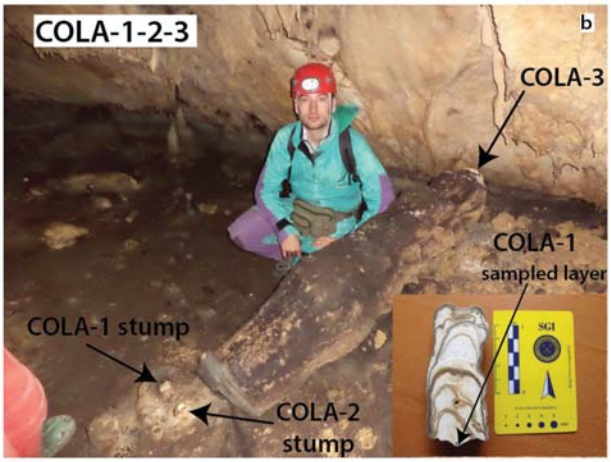
COLA-1-2-3
b
COLA-3
COLA-1
sampled layer
COLA-1 stump
COLA-2
stump

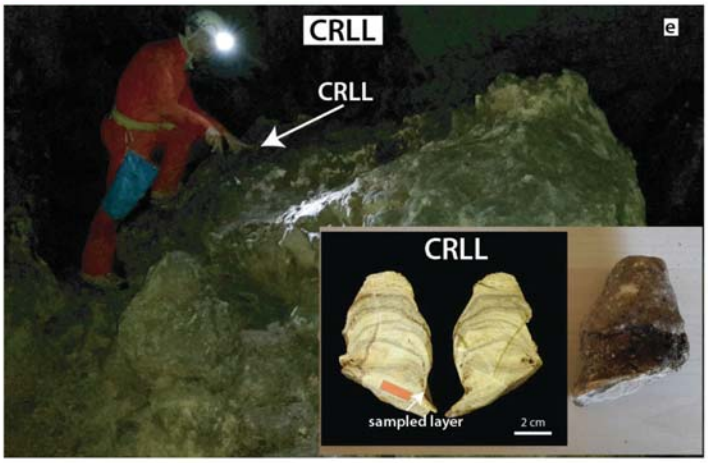
CRLL
e
CRLL
CRLL
sampled layer
2 cm

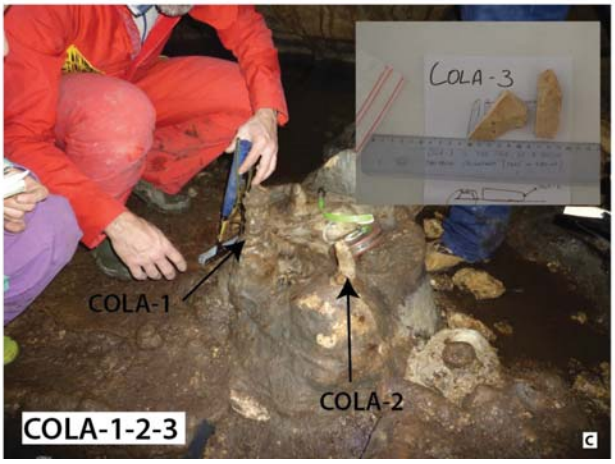
COLA-3
COLA-1
COLA-2
COLA-1-2-3
c

Figure 5.

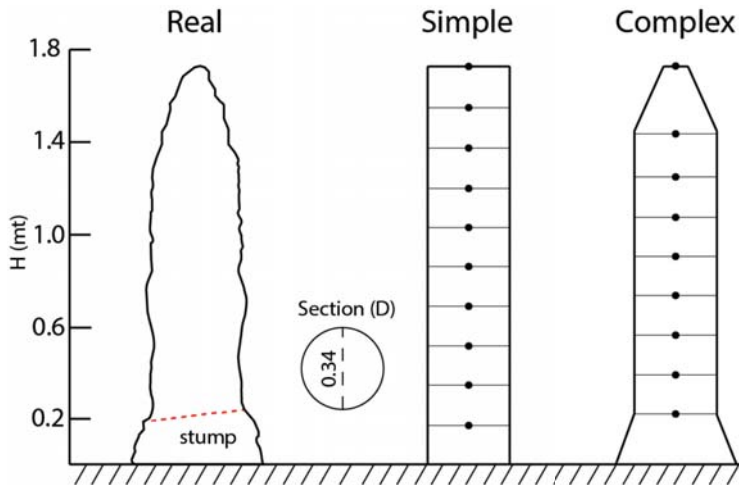
Real
Simple
Complex
1.8
1.4
1.0
0.6
0.2
H (mt)
Section (D)
0.34
stump

Figure 6.

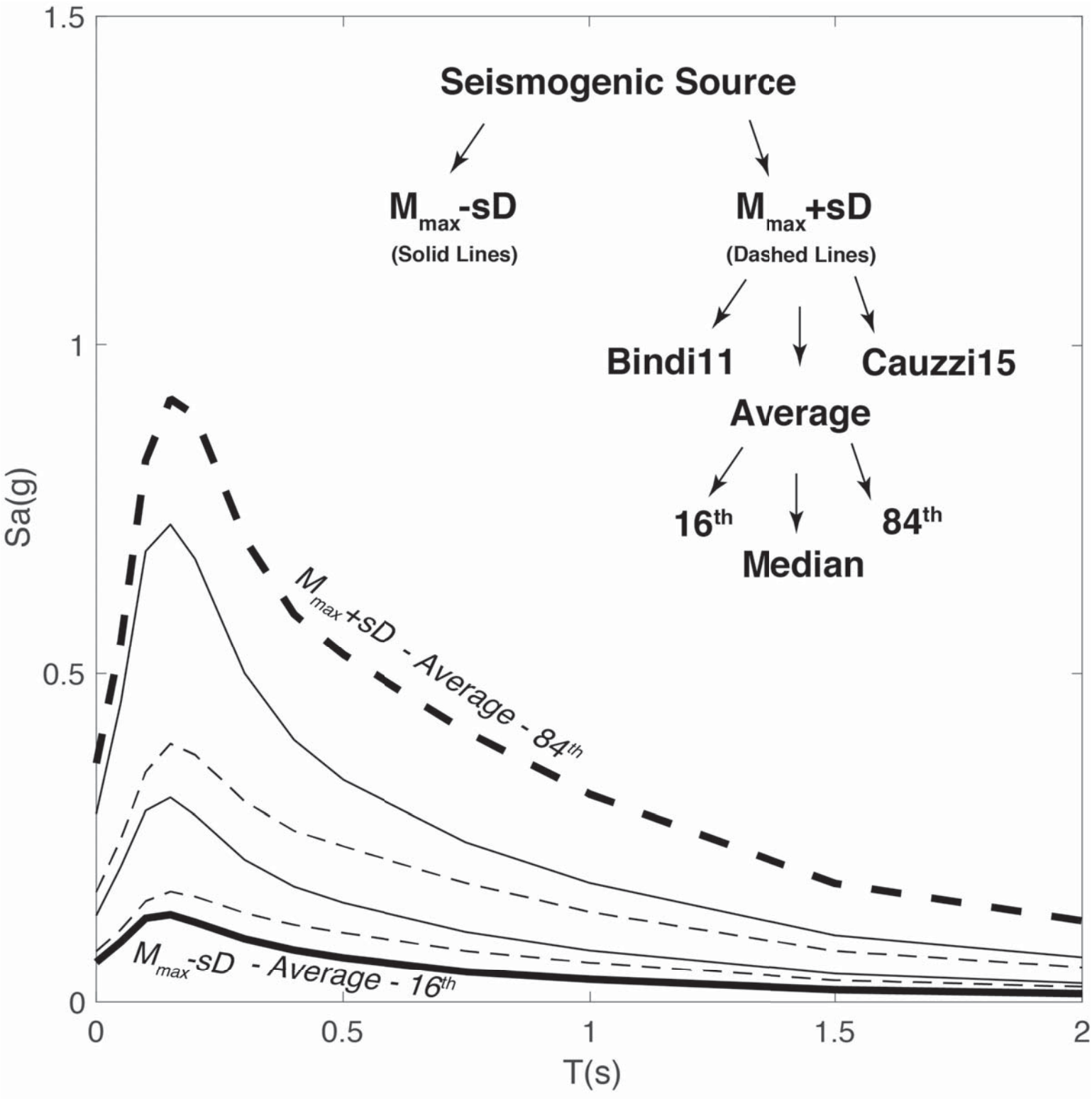
Seismogenic Source
Mmax-sD
(Solid Lines)
Mmax+sD
(Dashed Lines)
Bindi11
Cauzzi15
Average
16th
Median
84th
Mmax+sD - Average - 84th
Mmax-sD - Average - 16th
Sa(g)
T(s)
0
0.5
1
1.5
2

Figure 7.

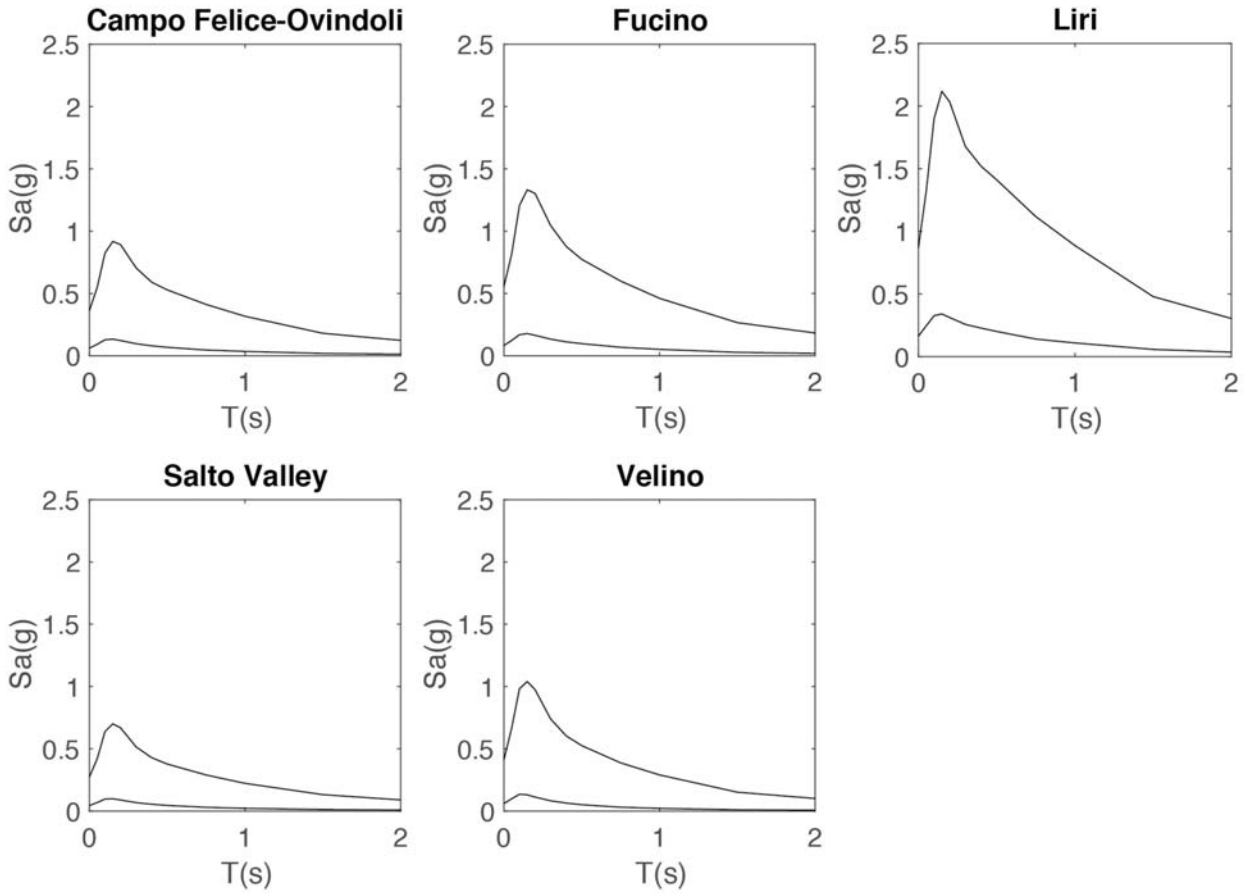
Campo Felice-Ovindoli
Fucino
Liri
Salto Valley
Velino
Sa(g)
T(s)
0
0.5
1
1.5
2
2.5

Figure 8.

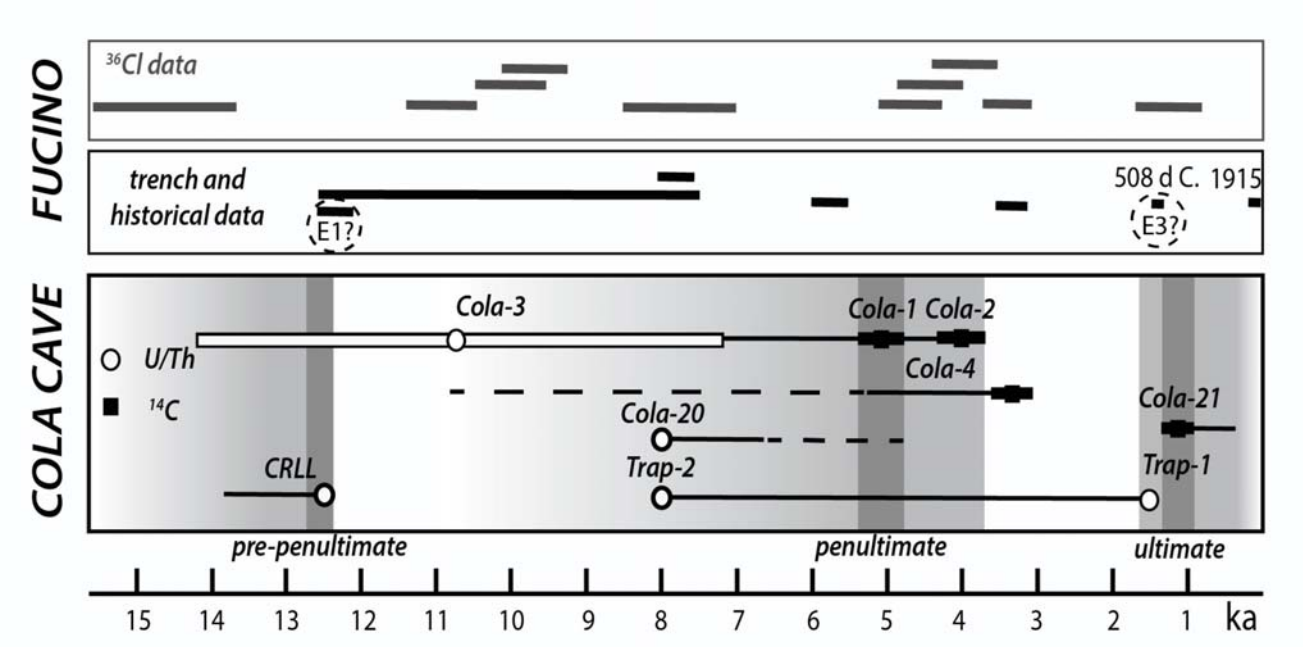
FUCINO
^{36}Cl data
trench and historical data
E1?
508 d C. 1915
E3?
COLA CAVE
U/Th
^{14}C
Cola-3
Cola-1 Cola-2
Cola-4
Cola-20
Cola-21
CRLL
Trap-2
Trap-1
pre-penultimate
penultimate
ultimate
15 14 13 12 11 10 9 8 7 6 5 4 3 2 1 ka

Figure 9.

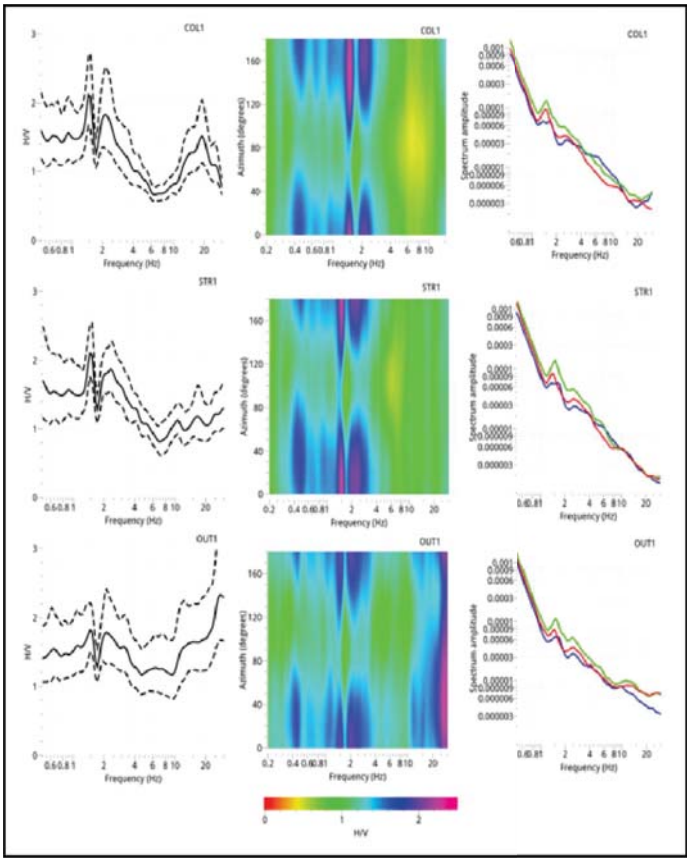
COL1
H/V
Frequency (Hz)
Azimuth (degrees)
Spectrum amplitude
STR1
OUT1
H/V

Figure 10.

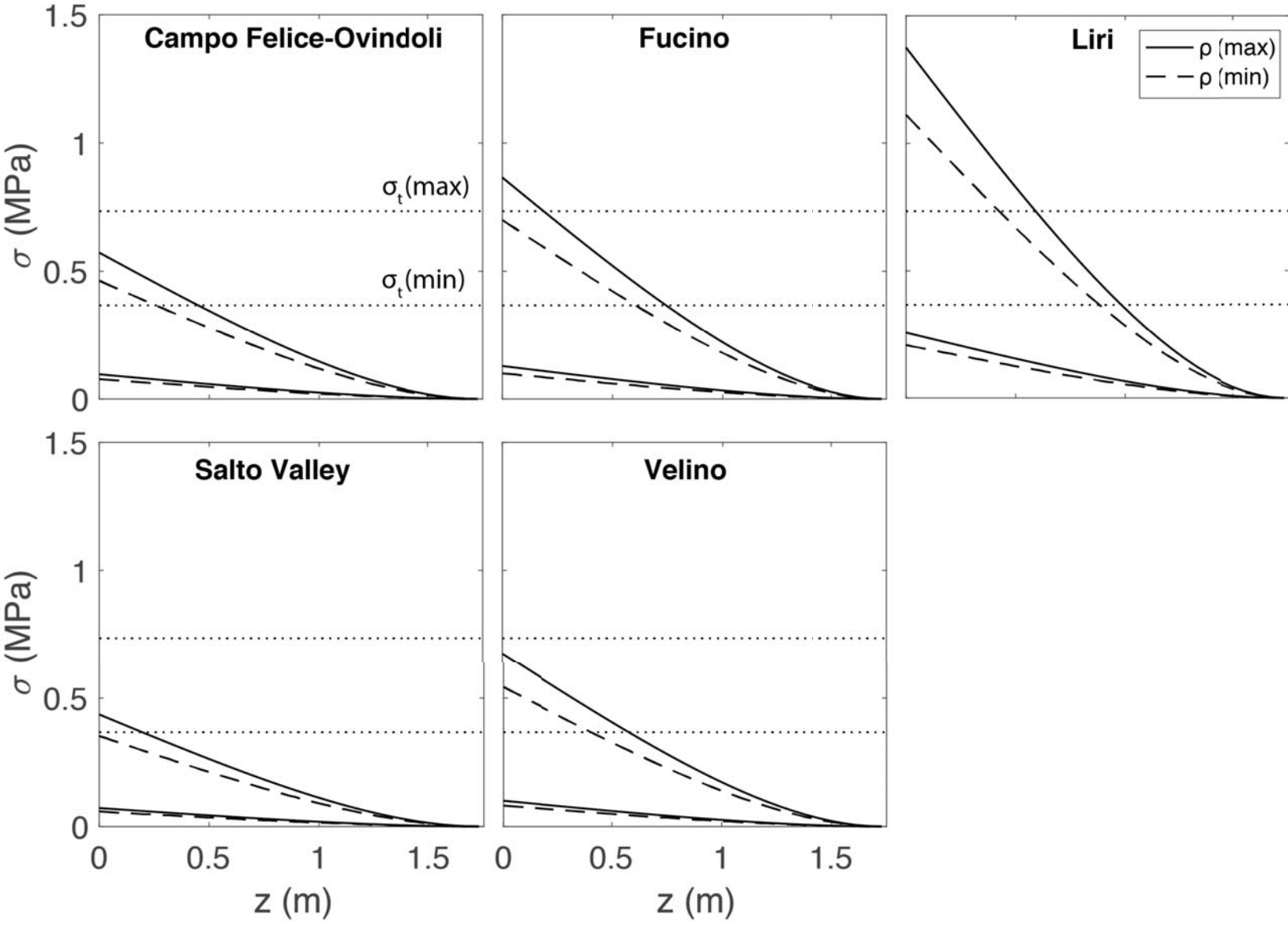
Campo Felice-Ovindoli
Fucino
Liri
Salto Valley
Velino
ρ (max)
ρ (min)
σ_t(max)
σ_t(min)
σ (MPa)
z (m)
0
0.5
1
1.5

Figure 11.

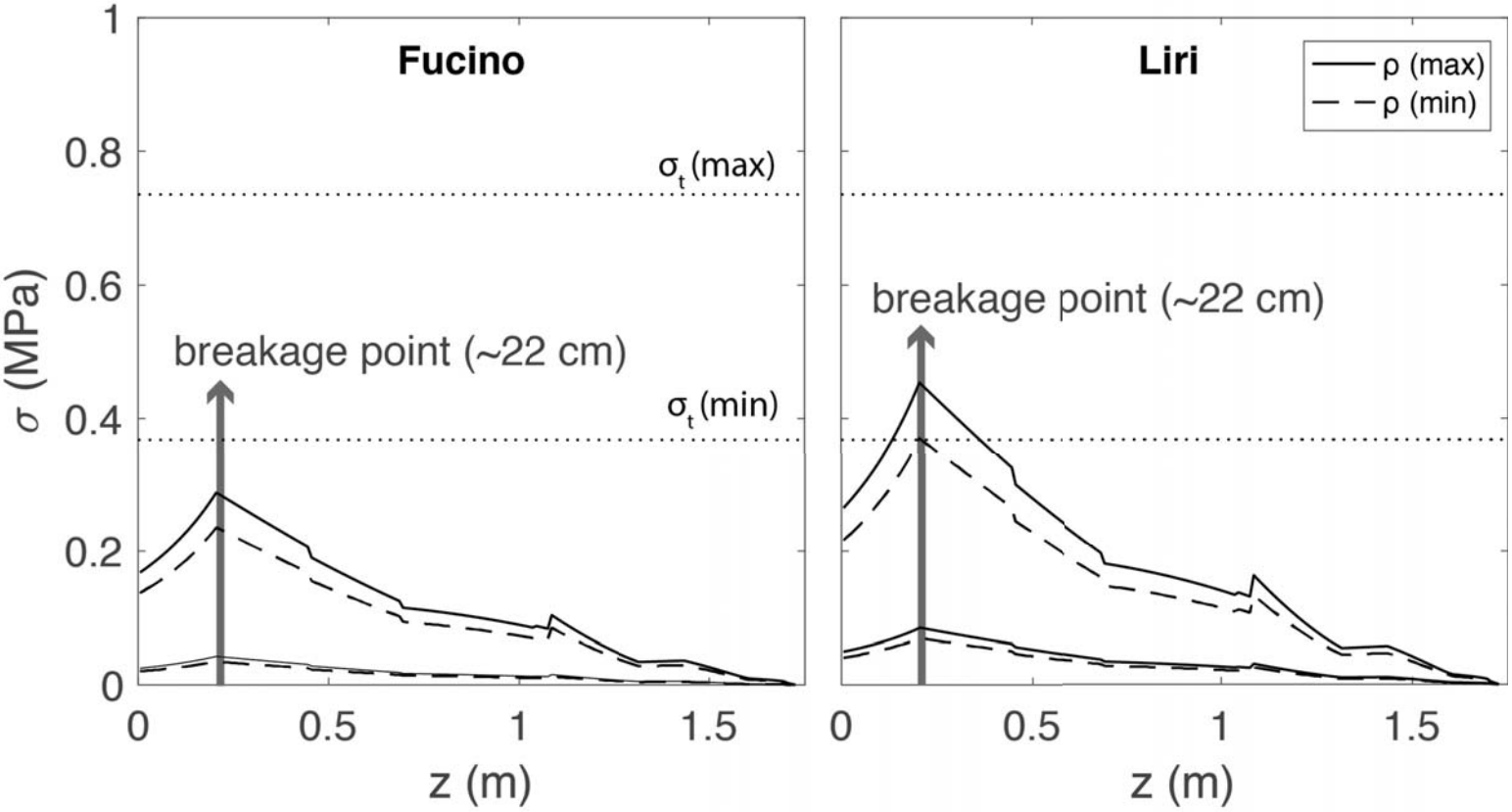
Fucino
Liri
ρ (max)
ρ (min)
σ_t (max)
σ_t (min)
breakage point (~22 cm)
breakage point (~22 cm)
σ (MPa)
z (m)
z (m)
0
0.2
0.4
0.6
0.8
1
0
0.5
1
1.5